A proposal of building new muon small wheels : the NSW project

Draft 2.00 09.09.2011

Abstract

abstract

1 Introduction [TK]

We propose to build a pair of new small wheel detector (NSW) to replace the existing ones during the second long shutdown[1] of the LHC during which the LHC will be upgraded to achieve its luminosity beyond the nominal design value and up to 2-3$\times 10^{34}$ cm^{-2}s^{-1} in the following running period. The goal of NSW is to bring a significant enhancement of the muon performance in the endcap region, in particular of the level-1 muon trigger as well as the precision muon tracking, that would not be achieved by simple and thus lower cost modifications alone such as improvement of radiation shielding, addition of new detector layers or upgrade of electronics.

The muon small wheel is a part of the ATLAS muon spectrometer located in the endcap region in front of the endcap toroidal magnet. This is the innermost station of the three muon stations of the endcap. There are two identical sets of detectors in both sides of ATLAS. The small wheel consists of 4+4 layers of monitored drift tubes (MDT) for precision tracking in the bending direction (R direction) and two layers of thin gap chambers (TGC) for azimuthal coordinates. These detectors cover the η range of $1.3 < |\eta| < 2.0$. The inner part of the small wheel is covered by four layers of cathode readout chambers (CSC) because of its high rate capability. Each CSC layers determines both bending and azimuthal coordinates. The coverage of the CSC chambers is $2.0 < |\eta| < 2.7$.

Just to check if reference works [1]. Once more to see the order is OK [2].

2 Upgrade motivations [TK]

Discussion of muon spectrometer performance at high luminosity - precision tracking and L1 trigger, and conclude that new detector and electronics are needed.

Point out serious (?) performance degradation in the small wheel region in both MDT and CSC, referring to the radiation background discussoin in Appendix. Performance of the present

[1] Currently it is foreseen in 2018.

detector should be evaluated for high lumi conditin, either using high lumi Monte Carlo or overlay of real events. CSC is 4 layers.

In the L1 discussion, emphasise the importance of maintaining low p_T threshold. There are two issues. the high rate of fake triggers in the endcap region based mainly on the study using data. Then introduce basic idea of how this can be mitigated by integrating the small wheel in the L1 trigger. As the second point of trigger, discuss the pT resolution and possible improvement using the new small wheel. Physics requirement asks low pT threshold (20-40 GeV), L1 rate should be maintained at 100 kHz. Need sharpening pT threshold. Here introduce 1 mrad requirement.

Finally conclude that NSW should be built and replace the present ones as a phase-1 upgrade item in preparation to running with luminosity beyond the nominal luminosity.

3 Requrements for the new small wheel [LP]

A short section with short subsections, summarising lists of requirements in numbers.

3.1 Tracking

Segment reconstruction with required performance. Resolution, efficiency, fake, ...

3.2 L1 trigger

Real-time segment reconstruction with required performance. Resolution, efficiency, fakes, ... Delay of signal availability.

3.3 Detector ageing

Integrated dose, Detector (and electronics) has to survive, or foresee replacement.

4 General Detector ..... [JD]

There are n proposed detector concepts which are discussed in next sections. Here, the following 3 points can be discussed commonly.

4.1 Mechanical structure

8+8 large-small layout, total space in z and R. Support structure, accessibility, ..

4.2 Radiation shielding

The same as now, or possible improvement of radiation shielding, ..

4.3 Alignment

Requirements, target figures, important comments which can be made independent of the detail of detector layout.

4.4 Readout electronics

Issues common to all concept. Around ROD.

4.5 DCS, services,

5 Detector concept 1 : MDT + TGC (working title)

5.1 Introduction

The dominant motivation behind the present proposal is to considerably increase the performance and rate capability of the triggering and precision tracking system in the Small Wheel in order to match the higher background levels in the phase II upgrade scenario of the LHC.

For this purpose, we propose the following layout for the upgrade of the Small Wheel.

(a) a new type of TGC trigger chamber, providing considerably improved spatial resolution in the bending plane but preserving the basic rugged structure together with the operating parameters of the proven TGC system, as presently installed in the muon end-cap.

(b) a new type of MDT chamber, made from tubes of half the diameter of the presently used tubes, otherwise operating under the same conditions with respect to gas gain, gas composition and pressure. The reduction of the tube diameter from 30 to 15 mm leads to an increase of the rate capability of the tubes by a factor of 7, sufficient to cope with the level of background hits expected at the SLHC.

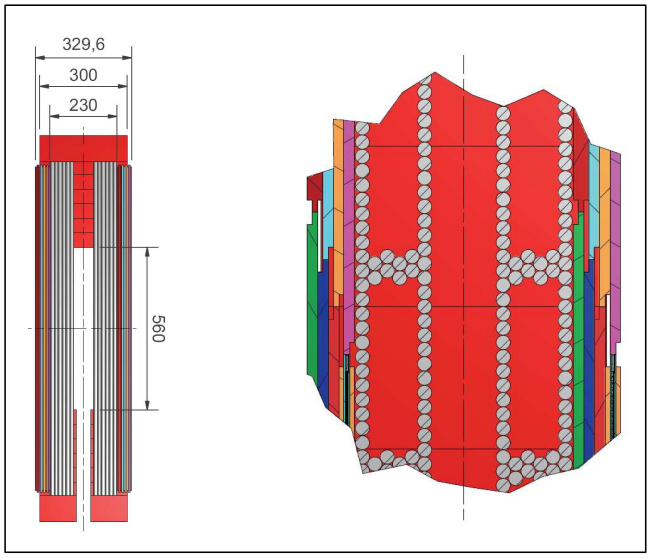

Figure 1: Cross section through the proposed arrangement of trigger TGCs and precision MDTs. The MDT, made out of two multilayers (with 4 or 6 tube layers) is sandwiched between two packages of 4-layer TGCs. The distance of 300 mm between the TGC packages is instrumental for the angular resolution of the triggering muon track.

With this upgrade of the existing chamber technology towards higher performance the uniformity of the present muon spectrometer (MDT as tracking detectors, RPC as trigger detectors in the barrel and TGCs in the end-cap) is preserved while profiting from the existing technical infrastructure and the experience to construct such an assembly at the relevant institutions.

For the trigger chambers we propose to maintain the basic operating concept of TGC chambers, complementing them with a new, high-performance readout system. The pulseheight distribution of signals induced into the strips of the TGC cathodes (measuring η) are convoluted to give the precision coordinate with an accuracy of <100 μm. To distinguish the new TGCs, proposed for the NSW from the existing ones in the Big Wheel, we will refer to them as to "sTGCs" throughout this article.

In the proposed detector layout, a package of 4 sTGC chambers is placed in front and behind the MDT chambers, each. A sTGC package will contain 4 wire layers (wires running radially, perpendicular to the strips), 4 cathode layers for centroide finding and another 4 cathode layers segmented into pads, for fast selection of a Region of Interest (Fig. 1). In the offline analysis the pads will be an important tool for resolving ambiguities in the x-y pairing of coordinates, when more than one track is present in a chamber.

One important limitation of the present L1-trigger in the end-cap is due to the fact that a majority of tracks crossing the Small Wheel do not originate from the primary vertex and should therefore not be considered candidates for a high-p_T muon by the triggering system. The present trigger, however, can not determine the slope of the candidate track in the r-z plane and for this reason is unable to discard tracks not coming from the primary vertex. With a distance of about 300 mm between the sTGC packages in front and behind the MDT, an angular resolution of $< 0,3$ mrad can be achieved, which allows to only consider tracks pointing to the interaction as high-p_T candidates for the L1 trigger. The slope of the track in the ϕ direction will also be determined, though with less accuracy, to further reduce the number of false triggers. A detailed presentation of the method is given in section 5.2.1.

The limitations of the MDT precision chambers at high luminosity are mainly caused by isolated hits in the tubes ("fake hits"), coming from neutron and gamma conversions in nearby support structures, tube walls, chamber gas and tungsten wires. The presently used 30 mm diameter tubes ("Large tubes") start to lose efficiency if hit rates go beyond about 300 kHz per tube and, therefore, a new MDT chamber type with half the tube diameter is proposed, leading to 7 times higher rate capability.

Both new chamber systems, the sTGCs and the MDTs, can be operated with the same chamber gas as in the present system. Power requirements for the electronics of both systems will be higher due to higher channel count. Whether this requires active cooling, as is now used for the electronics of the CSC chambers in the region $\eta > 2$ is under study. Aim is to have services arranged in such a way as to be able to use the existing service infrastructure like e.g. the cable Schlepps.

5.1.1 Upgrade of the TGC System

The basis of the proposed concept is to have as many as possible accurate measurements in the trigger layers, to allow to discard a high percentage of measurements where δ-rays, additional γ's or neutrons are present and still obtain a position measurement from each of the two packages with a precision of 100μm. To obtain such a precision using the 3.5mm pitch strips present in each gas-gap, while keeping simple electronics, a charge extrapolation method using Time-Over-Threshold as an approximated charge measurement has been developed. The achieved

performance using this method for large size sTGCs is discussed in detail in 5.2.

Achieving this high accuracy for the bending coordinate in each of the gas gaps allows the TGCs to provide a very good complement to the MDT measurements (of similar precision) and reduce the number of tubes. In particular, in the high background rate region of the Small Wheel, having a total of 16 potential measurement points, of which up to 30% may have to be discarded, ensure that an accurate particle vector will be provided in front of the End-Cap Toroidal field, even if some of the layers become non-operational during the exploitation of ATLAS at SLHC. The overall signal processing to produce the trigger is schematically shown in figure 38 of the appendix (C.1). A demonstrator to study the signal path, logics and latency in detail has recently been completed.

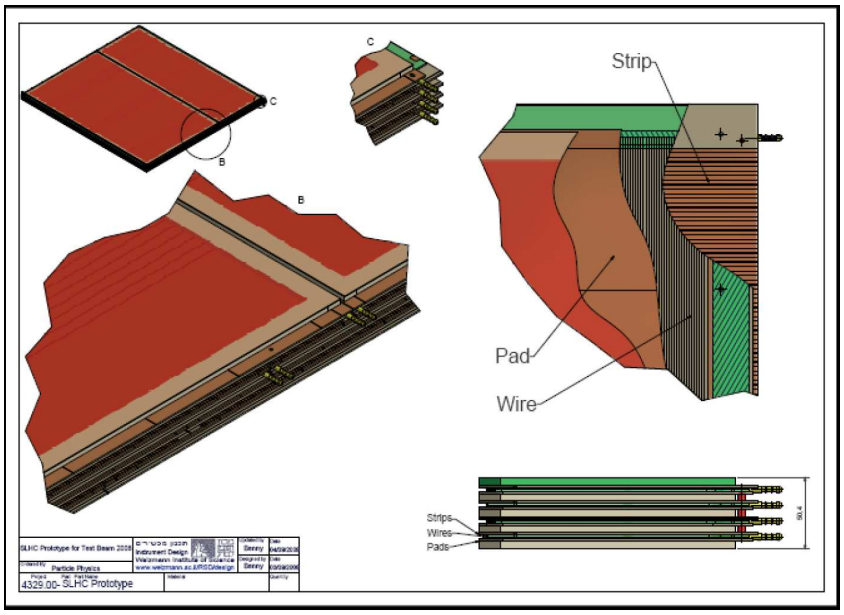

Figure 2: Schematics of the internal layout of a 4-layer TGC package, showing the pad-strip and wire readout for each gas-gap.

By making a coincidence among the pads in successive layers (within a 1 deg aperture), one is able to reduce substantially the number of channels that have to be readout for a fast trigger decision. Furthermore, the pad-coincidence provide a unique 3-D address, where a corresponding angle and displacement comparison can be made with the trigger input of the normal muon end-cap trigger originated in the ATLAS big wheels.

To simplify the logic of what channels to read for trigger purposes, one might loose some of the potential muon candidates, which can be recuperated by the measurements of the MDT (smaller number of channels). The MDTs provide, furthermore an accurate alignment that can be used to align with tracks the exact TGC positions.

5.1.2 Upgrade of the MDT System

As mentioned above, the large majority of hits in the Monitored Drift Tubes (MDT) are caused by Compton scattering of γ's which, in turn, come from neutron capture in the material

of the chambers and adjacent support material. The resulting hit densities strongly increase towards the inside of the Small Whell, while, on the other hand, the length of the tubes in the trapezoidal geometry of the SW decreases proportional to the distance from the beam line (r). As hit densities, however, are increasing considerably faster than with 1/r, the highest tube hit rates are at the innermost radii of the chambers.

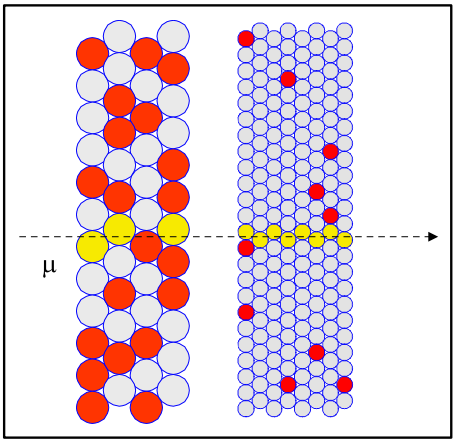

Figure 3: The tracking quality in 30 mm and 15 mm drift tubes in a region of high n/γ background. The occupancies from background hits (red dots) are 50% in the 30 mm tubes but only 7% in the 15 mm tubes due to shorter drift time and smaller area.

Table 1 presents tube hit rates, occupancies and efficiencies for the innermost tubes of the 4 chambers in a Large Sector of the NSW. Chamber EIL0 covers the area now taken by the CSC. EIL3 is the small rectangular extension at the outside of the sector. The numbers in col. 4 are based on hit rate measurements at a luminosity of $9 \cdot 10^{32}$ cm^{-2}s^{-1}, scaled up linearly to $5 \cdot 10^{34}$ cm^{-2}s^{-1}. Rates in the CSC region (1 m<r<2 m) are extrapolated from larger radii, using an exponential law [22]. In addition, a factor of 1,7 has been applied to increase rates to the 9 kHz/cm^2 specification of this Technical Proposal. This could also be considered an additional safety factor in case the real rates will increase faster than predicted by the extrapolation. The efficiencies are calculated from exp(-τ·f) $\approx$ 1-τ·f, where τ is the dead time after a hit (we use the maximum drift time of 200 ns) and f the hit rate per tube.

Chamb. type	Tube layers	Location in r	Tube length	Expected hit rate	Count rate per tube	Occup-ancy	Tube effi-ciency	Segment efficiency
		cm	*cm*	*Hz/cm^2*	*kHz*	*%*	*%*	*%*
EIL0	2×6	93	56	9000	756	15,1	86,0	99.9
EIL1	2×4	208	125	3309	620	12,4	88,3	99.9
EIL2	2×4	318	179	1271	341	6,8	93,4	99.9

Table 1: Expected hit rates and efficiencies for 15 mm tubes in a large sector of the NSW. In col. 3 the radial location of the innermost tube of each chamber and in cols. 4 to 8 the tube lengths, the expected hit rates, the counting rates per tube, the occupancies and the 3σ single-tube and the track segment reconstruction efficiencies of a chamber are given for the tubes with highest counting rate at a luminosity of 5 × nominal (times a factor of 1,7, see text).

Reduction of the outer drift-tube diameter from 30 mm to 15 mm, while keeping the other parameters unchanged (gas composition and gain, sense wire diameter and tube wall thickness,

see Table 2) leads to a significant improvement of the rate capability of the drift-tube chambers, more than sufficient for their operation in the New Small Wheels up to the highest background rates expected at 5 times the LHC design luminosity. This improvement is illustrated in Fig. 3.

Being able to use MDT at very high rates allows to preserve the main advantages of the drift tube concept:

(a) High pattern recognition and tracking efficiency, even at high backround rates.

(b) High position and angular resolution, independent of the angle of incidence onto the chamber plane. This property of the *circular* drift geometry of chambers made from tubes is a decisive advantage over drift chambers with *rectangular* drift geometry.

(c) Operational independence of the drift tubes, where a malfunction of any individual tube can only generate a negligible inefficiency.

(d) Modularity and mechanical robustness of chamber construction.

(e) Direct connection of the high intrinsic mechanical precision of the chambers to the global optical alignment system.

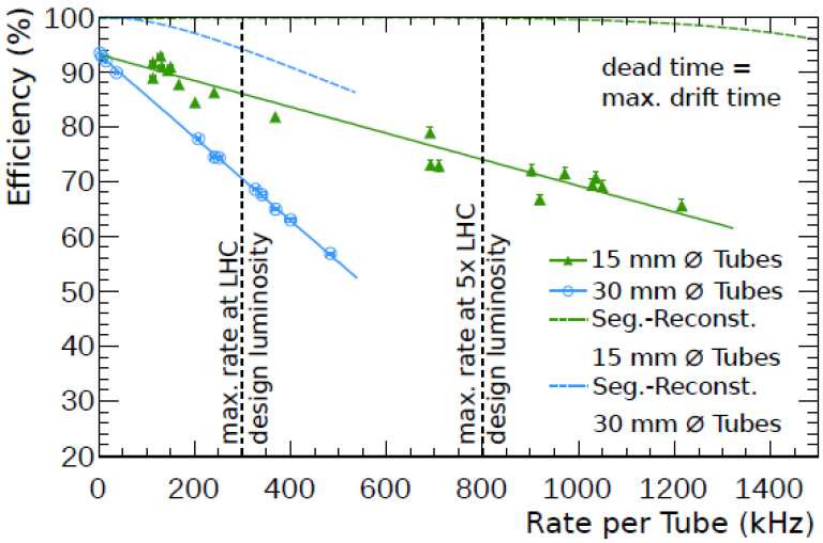

Figure 4: Track segment reconstruction efficiencies as a function of the background counting rate for different numbers of tube layers calculated requiring at least 4 hits on the track and using the measured 15 mm diameter single-tube efficiencies as a function of the counting rate for finding a hit within $3\sigma_r$ distance from the track (3σ efficiency) where σ_r is the drift tube spatial resolution.

For the standard MDT gas mixture of Ar:CO_2 (93:7) at 3 bar absolute pressure, the gas gain of $2 \cdot 10^4$ is achieved at an operating voltage of 2730 V for 15 mm diameter drift tubes (Table 2). Under these operating conditions, the maximum drift time is reduced by a factor of 3.5 from about 700 ns to 200 ns [14]. In addition, the background flux, hitting a tube of given length is reduced by a factor of two. Altogether, the drift-tube occupancy is thus reduced by a factor of 7. At a background rate of 9 kHz/cm^2, the expected maximum at the innermost

radius of the Small Wheels at 5 times the LHC design luminosity, the highest occupancy is 15 %, corresponding to a counting rate of 750 kHz (cf. Table 1). The 2×6 drift-tube layers at radii $R < 2$ m in the Small Wheels and 2×4 layers at larger radii provide very robust tracking with track segment reconstruction efficiencies above 99 % up to the highest background rates (Fig. 4) [17]. In this configuration, the point and angular resolution of the drift tube chambers will be uniformly 45 μm and 0.5 mrad, respectively, compared to 40 μm and 0.45 mrad without background irradiation.

Parameter	**Design value**
Tube material	Aluminum
Outer tube diameter	14.97 mm
Tube wall thickness	0.4 mm
Glue gap between tubes	0.1 mm
Wire material	Gold-plated W/Re (97/3)
Wire diameter	50 μm
Gas mixture	$Ar/CO_2/H_2O$ (93/7/$\leq$ 1000 ppm)
Gas pressure	3 bar (absolute)
Gas gain	2 x 10^4
Wire potential	2730 V
Maximum drift time	$\sim$ 200 ns
Average resolution per tube	$\sim$ 100 μm

Table 2: The operating parameters for small-diameter MDTs.

The design of the mechanical structures and of the alignment system follows as closely as possible the one for the present Small Wheel architecture. Like in the case of the TGCs, faster readout electronics will have to be installed (see section 5.5).

5.2 Detector technology and layout

5.2.1 Detector technology and layout of the sTGC chambers

The structure of the new sTGC chambers is given in Fig. 10, while the schematic layout of the proposed detection system is shown in Fig. 6. It should be consider as one of the possible arrangements of identical small-large sectors. The 8-layer small tube MDTs are sandwiched between two sTGC packages, each 5 cm thick, containing 4 gas-gap each. Each gas-gap provides pad-strip and wire readout. Since the trigger chambers, unlike the MDT, do not need an overlap region for relative alignment, that part of the MDT surface is used to implement the alignment connection (purple boxes) to the projective alignment bars. The internal structure of each sTGC package is the same as that shown in Fig. 1. The innermost radial sTGC package are subdivided into two stair-like packages (to provide full coverage in 3 out of 4 layers), in order to keep short wires in the high background region. The readout of the wires is done as an OR of the segments, flagged by the corresponding pad coincidence. The preliminary dimensions of each sTGC package can be seen in Fig. 6. This corresponds to a total 192 packages, each of them containing 4 gas-gaps, corresponding to a total of 768 gas-gaps.

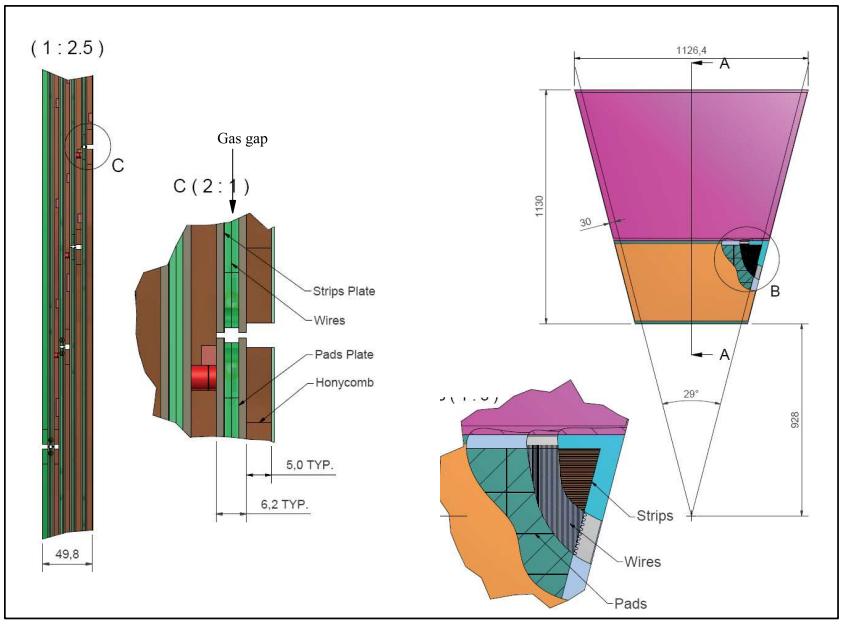

Figure 5: Construction of a TGC chamber.

The corresponding number of electronics channels is given in Table 3, where the pad surfaces increases from $7.5\times7.5\text{cm}^2$ to $20\times20\text{cm}^2$ at the outermost radial layers. The surface of the pads are determined by the corresponding background rates. The pads would be shifted every two layers (Fig. 7) to reduce the size of the corresponding Region-of-Interest (ROI), from which the strips (wires) will be digitized and used for trigger.

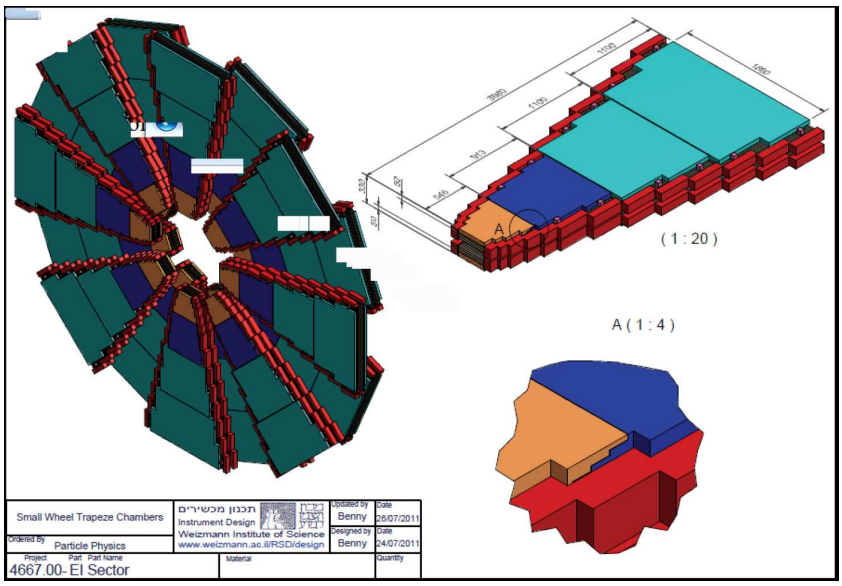

Figure 6: Schematic of the detector layout for the case of equal small-large sectors. Insert A shows the stairs-type arrangement for the innermost radial sTGC package. The purple boxes represent the alignment elements for the MDT detectors.

The internal alignment achieved by the production of the strip patterns in the sTGC gas gap is precise to within less than 50 μm, however the transfer of this precision from gap-to-gap has only been achieved to within better than 150 μm. For this reason, the final precision

alignment between gaps will be done using tracks from the sandwiched MDT. This requires very few tracks, since the internal strip pattern within a gap is extremely precise.

The mechanical stability of a TGC package is very good for vertically mounted detectors, based on the ATLAS experience. The use of composite materials allows for very small sensitivity to temperatures (in particular within the range of the temperatures in the small wheel), as well as no sensitivity to the magnetic field in the Small Wheel region. To be able to achieve this lack of sensitivity, the mounting needs to be kinematic (one fix point, one sliding point and one plane), of the same type as presently used in ATLAS.

The processing of the sTGC signals is considerably more complex than for the existing TGCs. An accurate determination of the track position in the two chamber packages has to be done, and the resulting vector has to be extrapolated to the corresponding trigger sector in the Big Wheel. In this process the overall latency must stay below the maximum allowed in the present ATLAS readout scenarion and in phase I. Details of the proposed readout scheme are given in 5.4.

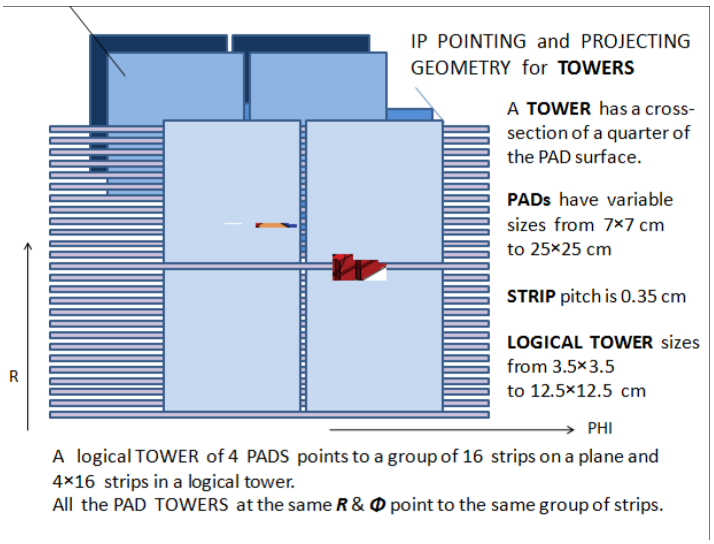

Figure 7: Schematics of Pad and strips arrangement (only 2 layers shown).

Each package will be connected to 4 HV lines, 3 LV lines and the corresponding optical fibers to transmit the trigger/data information. The HV lines will be connected to one corner of the chamber, while the LV and fibers will be connected to a trigger box, where the logic will be installed. In case of a major failure, the full TGC-MDT-TGC package will be replaced. This means that 2 such spare packages for each of the station types need to be constructed.

Component	Number of channels
Strips / side	135,000
Pads / side	30,000
Wires / side	27,500
For two sides detector	385,000

Table 3: Channel distribution for the 3 readouts for the 192 packages containing 768 gas gaps.

5.2.2 Detector technology and layout of the sMDT chambers

Figure 8: Structure of the NSW for the sMDT-sTGC system.

Figure 9: Layout of the sMDT and sTGC chambers in the large sectors of the NSW.

Figure 10: Layout of the sMDT and sTGC chambers in the small sectors of the NSW.

The layout of the sMDT chambers for the NSWs follows exactly the present layout of the MDT chambers in the Small Wheels with fully projective small and large chamber towers in combination with the EM and EO layers (see Figs. 8-??). The chamber parameters are summarized in Table 4. There are only three radial chamber segments in each sector. The sTGC chambers are precisely positioned and kinematically mounted on the outer tube layers of the sMDT chambers on both sides. The integrated sMDT-sTGC chamber packages are connected by light rays to the global optical alignment system and with the neighbouring chambers via sensors mounted precisely on the outer tube layers of the inner multilayers of the sMDT chambers while the in-plane alignment system is integrated into the sMDT spacer structure which also carries the common chamber supports. The well understood alignment system implementation guarantees precise absolute chamber alignment from the beginning which is essential for the performance of the muon spectrometer.

sMDT chambers	EIL0	EIL1	EIL2	EIS0	EIS1	EIS2
Number of chambers	2 x 8	2 x 8	2 x 8	2 x 8	2 x 8	2 x 8
Radial extension (mm)	1095	1095	1457	1215	1276	1095
Minimum chamber width (mm)	740	1428	1968	678	1056	1434
Maximum chamber width (mm)	1380	1878	2418	1002	1380	1704
Minimum tube length (mm)	560	1248	1788	498	876	1254
Maximum tube length (mm)	1200	1698	2238	822	1200	1524
Spacer height (mm)	68	120	120	68	120	120
Thickness in z, tubes (mm)	228	228	228	228	228	228
Thickness in z, chamber (mm)	300	300	300	300	300	300
Weight/chamber (kg)	150	130	180	140	120	130
Number of tube layers	2 x 6	2 x 4	2 x 4	2 x 6	2 x 4	2 x 4
Number of tubes/layer	72	72	96	80	84	72
Number of tubes/chamber	864	576	768	960	672	576
Total number of tubes	13824	9216	12288	15360	10752	9216
Gas volume/chamber (l)	122	162	219	102	110	127

Table 4: Parameters of the sMDT chambers in the NSWs. The total number of drift tubes is 70656 and the total gas volume in each NSW 6750 l.

The design of the muon drift-tube chambers with 15 mm diameter tubes for the new Small Wheels follows as closely as possible the current ATLAS MDT chamber design in the endcap region of the muon spectrometer (Fig. 11). The chambers consist of two multilayers of four or six layers of drift tubes each in densest package. The aluminum tubes of 15 mm outer diameter and 0.4 mm wall thickness are produced according to industry standard and are chromatized

for cleaning and reliable electric contact. The tubes are separated by 0.1 mm wide glue gaps during chamber assembly. The two multilayers are separated by a spacer frame carrying the supports of the integrated drift-tube and trigger chambers on the Small Wheel structure and the in-plane optical alignment system monitoring the planarity of the chambers. The aluminum spacer frame is of similar design as for the present Small Wheel MDT chambers. The main changes in the chamber design are due to the four times denser packaging of the drift tubes and their gas and electrical connections.

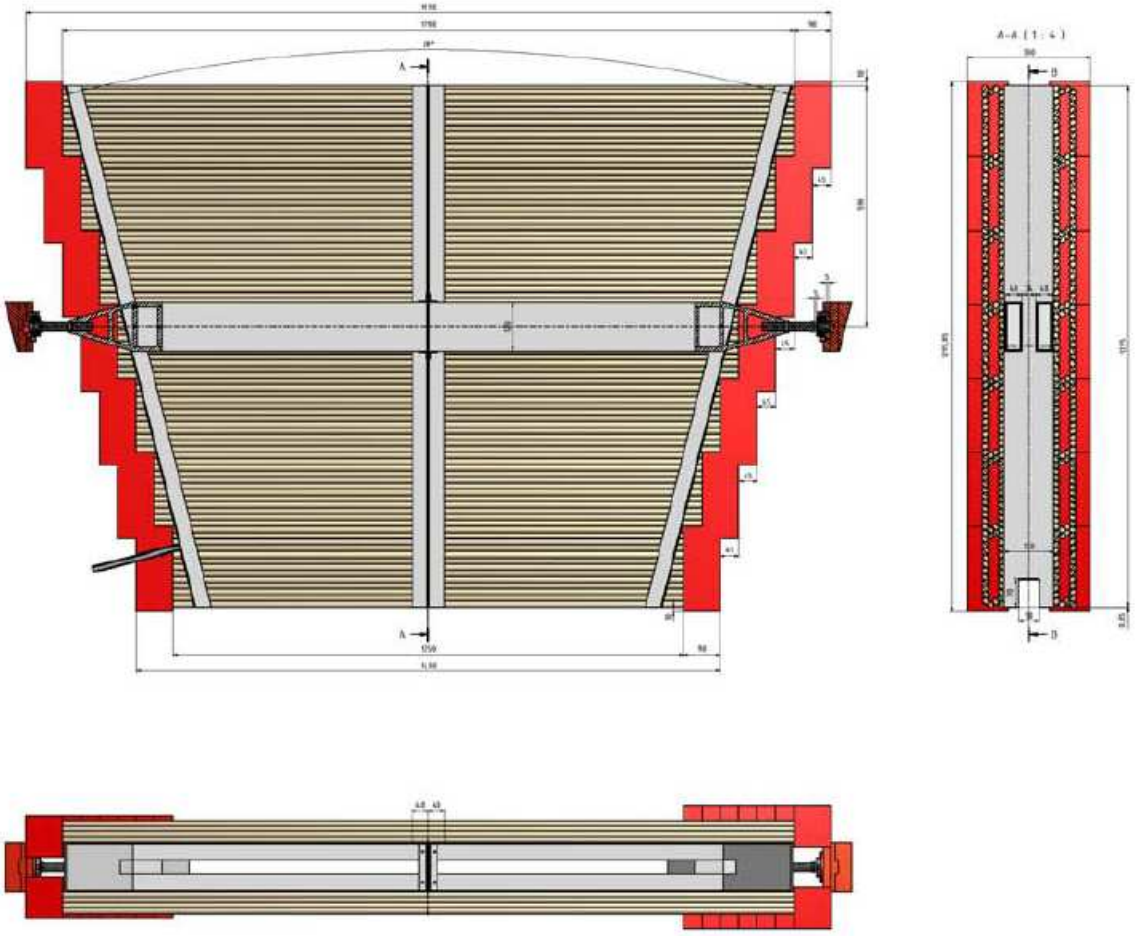

Figure 11: Small drift-tube chamber design for the new Small Wheels. The integration with the trigger chambers is also shown.

Central to the chamber design is the design of the drift tubes and of their endplugs (see Fig. 12). The aluminum tubes of 15 mm outer diameter and 0.4 mm wall thickness are produced according to industry standards (DIN) with tolerances of ± 0.1 mm on diameter, roundness and concentricity of inner and outer circumference and of ± 0.5 mm on straightness and chromatized for cleaning and reliable electric contact. The endplugs insulate the sense wire from the tube wall, center the wire in the tubes, position it with respect to the external reference surface on the endplug with an accuracy of better than 10 μm and provide high-voltage-safe connections to the gas distribution manifold (see Figs. 13) and to the 24-channel readout and high-voltage interface boards ("hedgehog cards", Figs. 27).

The wire is fixed at both tube ends in copper crimping tubes inserted into the central brass inserts of the endplugs and connected to the signal and high-voltage hedgehog cards via brass signal caps which are screwed onto the brass inserts, sealing the tubes with respect to the gas manifold with O-rings. The brass insert of the endplug holds the spiral-shaped wire locator ("twister") in a central bore on the inside of the tube and transfers the wire position to the precisely machined reference surface at the outside of the tube which is used to accurately position the drift tubes during chamber assembly. The wire position information is transferred solely via the precision machined brass insert; precision machining of the complete endplugs is not necessary anymore, facilitating the production of the tubes and improving the accuracy of chamber construction. The two most critical problems for the ATLAS MDT drift tube production, cracking of the Noryl® plastic insulator and precision machining of the injection moulded endplugs, have been eliminated by the new design.

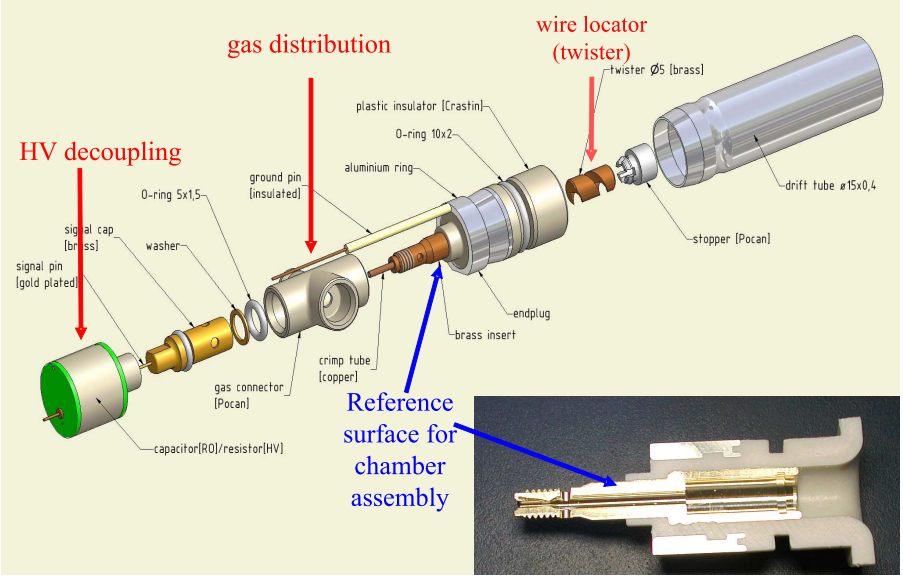

Figure 12: Exploded view of a drift tube with gas connection, signal and ground connection and encapsulated high-voltage decoupling capacitor.

The insulators of the endplugs consist of Crastin®, a PBT based thermoplastic with 30 % glass fiber admixture to improve mechanical stability which shows little shrinkage and outgassing and, unlike Noryl® (material in the present MDT endplugs), high stability against cracking under stress. The material is of similar chemical composition as Pocan® which is used for the injection moulded components of the gas manifolds of the present and the new drift tube chambers. The endplugs are fabricated by injection moulding and sealed in the aluminum tubes with O-rings by circular mechanical crimping of the tube walls.

The modular gas distribution system consists of injection moulded plastic tubes made of Pocan® without glass fiber which interconnect adjacent tubes in the direction perpedicular to the multilayer and connect them to an aluminum gas distribution bar on the readout and the high-voltage end of the multilayer.

The readout and high-voltage supply scheme follows closely the one of the present MDT chambers using the same parameters and specifications. The high-voltage decoupling capacitors on the readout side and the terminating resistors on the high-voltage supply end are individu-

Chamb. type	Tubes× layers×MLs	Tubes/ chamber	Tubes total	Mezz.cards/ chamber	Mezz.cards total	CSMs/ chamber	CSMs total
EIL0	$72 \times 6 \times 2$	864	13824	36	576	2	32
EIL1	$72 \times 4 \times 2$	576	9216	24	384	1	16
EIL2	$96 \times 4 \times 2$	768	12288	32	512	2	32
EIS0	$80 \times 6 \times 2$	960	15360	40	640	2	32
EIS1	$84 \times 4 \times 2$	672	10752	28	448	2	32
EIS2	$72 \times 4 \times 2$	576	9216	24	384	1	16
Total side A + C:			70656		2944		160

Table 5: Electronics Channels (drift tubes) and readout boards in the NSW. Each mezzanine card serves 24 drift tubes, matching the modularity of the chambers with 6 and with 4 tube layers per multilayer, and each CSM 24 mezzanine cards.

ally encapsulated in plastic containers for high-voltage protection. The plastic containers are integrated with the hedgehog cards plugged onto the gold-plated pins of the signal caps and ground connectors. The ground pins are screwed into the gaps formed by three adjacent tubes In order to during chamber assembly to connect the tube walls to the ground of the hedgehog cards. This scheme allows for the high-voltage-free design of the readout hedgehog cards. Each readout hedgehog card carries a mezzanine card with the new radiation hard active readout electronics (see below). The mezzanine cards follow the shape of the hedgehog cards and are currently under development. The electronics boards are enclosed in aluminum Faraday cages which also shield the readout hedgehog cards against the mezzanine cards. The modularity of the sMDT chambers in the NSW is given in Table 5.

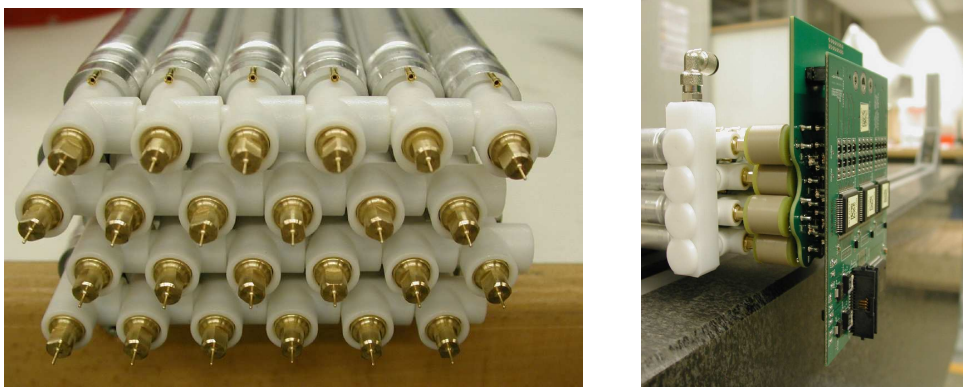

Figure 13: Left: The gas manifold for the Small tube chambers. The gas distribution is integrated into the endplug design. No gas bar with separate connections to each tube is needed. Right: The HV-coupling capacitors, housed in small plastic cylinders, are directly plugged onto the signal pins. In the next layer: signal distribution ("hedgehog") and frontend electronics ("mezzanine card").

The modular gas distribution system consists of injection moulded plastic tubes made of Pocan® without glass fiber which interconnect adjacent tubes in the direction perpedicular to the multilayer and connect them to an aluminum gas distribution bar on the readout and the high-voltage end of the multilayer.

5.3 Performance

Summary of chamber performance, details in appendix of technology.

Spatial and angular resolution as functions of rate and angle of incidence
Time resolution
Efficiency (single measurement and segment)
Double track resolution
Rejection of fake and background tracks

5.3.1 Performance of the sTGC trigger chambers

The most important issue for a detector that needs to operate at high rate during a period of more than 10 years, is its aging characteristics. For this reason, a series of small TGCs (10 $\times$ 10 cm^2) detectors were constructed and exposed to γ irradiation for various periods of time. No deterioration was observed in any of these prototypes. The one with the longest exposure was opened after a total irradiation of 6 Cb/cm of wire (i.e. 33 Cb/cm^2). Fig. 14 shows the rate and current behavior of the detector during the irradiation. No noticeable degradation is observed after the MIP dose equivalent to 2,000 days of operation at the hottest location in the ATLAS Small Wheel.

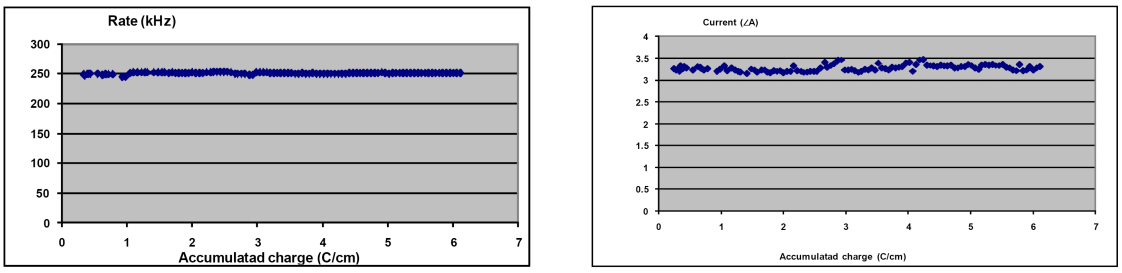

Figure 14: Counting rate and current as a function of the integrated charged in the detector.

The irradiated detector was opened to see the effect of the irradiation. Fig. 15 shows a microscope picture of a wire in the irradiated region, as well as in the non-irradiated region. The deposits in the irradiated region were analyzed, the deposits being mainly Carbon and Oxygen, as expected from the gas composition.

In order to perform the R&D needed for the use of TGCś in the ATLAS Small Wheels, six large (ranging from 120$\times$100 cm^2 to 70$\times$40cm^2) packages of TGCs, each one containing four gas-gaps, each gap with pads-strips and wire readout, have been constructed. These detectors were irradiated in various facilities to evaluate their behavior and position resolution. The time, position and angular resolutions were determined from measurements performed in the H8 facility at CERN, while the efficiency for MIPś under a high full area irradiation with $\gamma^{'}$ s was performed at the SOREQ Nuclear Center (Israel) using Co(60) source, while triggering on cosmic muons.

The sensitivity to neutrons was measured at the Demokritos Nuclear Center (Greece). To

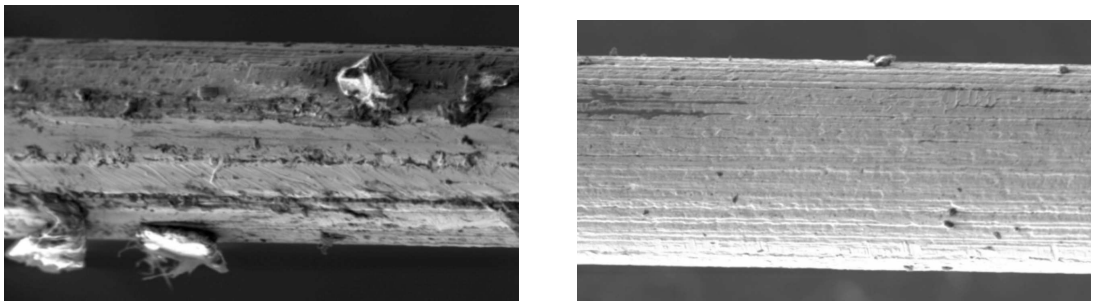

Figure 15: Deposits observed in the irradiated (left) and non-irradiated region of a wire.

simulate the present proposal, the trigger used at the H8 test-beam was the expected 3-out-of-4 coincidence of pads. The time resolution of this trigger with respect to a beam-defined scintillator is shown in units of 0.8 ns in Fig. 16 (left). It can be seen that the time resolution of the system is able to provide the bunch crossing identification with high efficiency.

Fig. 17 shows the individual efficiencies of each of the layers for Pads, Strips and wires of one such package, using the Time-over-Threshold method. It can be see that they are all fully efficient at an operating voltage of 2.9 kV, which was used for the rest of the tests.

The position resolution of each individual gap was measured by using clean muon tracks in the small tube MDT test detector that was part of the test beam set-up. The strip multiplicity distribution that provides the charge centroid is shown in Fig. 16 (right).

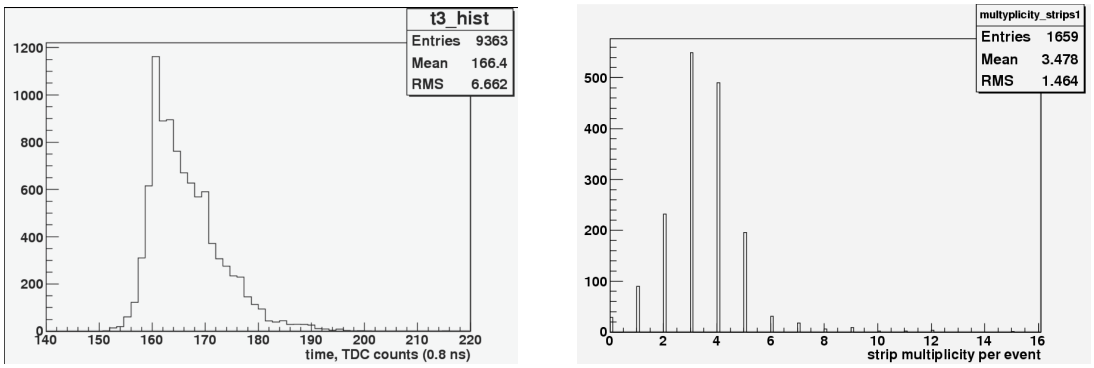

Figure 16: Left: Time difference between 3-out-of-4 pad trigger with respect to the beam scintillator in units of 0.8 ns. The FWHM is 11 ns. 99% of the distribution is within 25 ns. Right: Strip multiplicity for a MIP on a typical gas gap.

The TGC position resolution was calculated from a fit to the difference between the measured position in a given layer and the position extrapolated from a fit to the other three layers, as shown in Table 6 (before and after the correction for inter-gap misalignment). A typical distribution for one layer is shown in Fig. 18. It can be concluded that the position resolution achieved with the TGC layers fulfills the requirements for the NSW and provides a valuable complement to the position measurements of the MDT.

The position resolution as a function of incident angle has been measured in the past using a regular ADC to determine the charge in each individual strip. This measurement will be

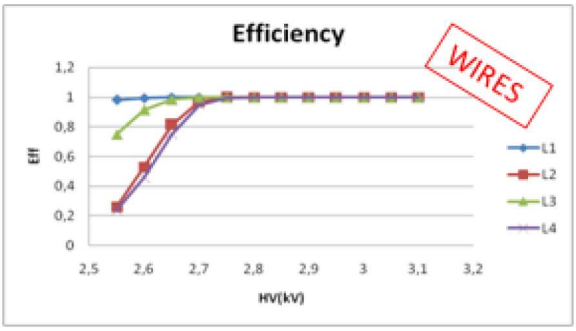

Figure 17: Plateau curve for each of the gaps used in the test, using the T-O-T method.

repeated in the August 2011 test beam using Time-over-Threshold. The dependence of the single layer resolution as a function of angle is shown in Fig. 19.

Layer	$\sigma_{corr}(\sigma_{nocorr}) \pm \Delta\sigma[\mu\text{m}]$
1	66.2 (120.9) $\pm$ 1.2
2	66.7 (79.8) $\pm$ 1.1
3	63.6 (76.0) $\pm$ 1.0
4	63.8 (116.49) $\pm$ 1.0

Table 6: Position resolution in the 4 layers after (before) correcting for individual layer position.

The angular resolution of a single sTGC package was obtained by comparing the angle between one package of sTGCś (4 gaps) with the one measured with the Small Tube MDT test chamber. The difference has a resolution of 3 mrad. Having such a resolution with a single sTGC package (5 cm thick) implies that with two packages separated by 300 mm, the angular resolution of the system would be better than 0.3 mrad at the Level-1 trigger.

The measured single layer efficiencies for MIPś in a γ background has been measured by triggering with cosmics under a high irradiation flux. The results are shown in Fig. 20, left. Similarly, this was done with 5.5 MeV neutrons. The corresponding single layer efficiency is shown in Fig. 20, right.

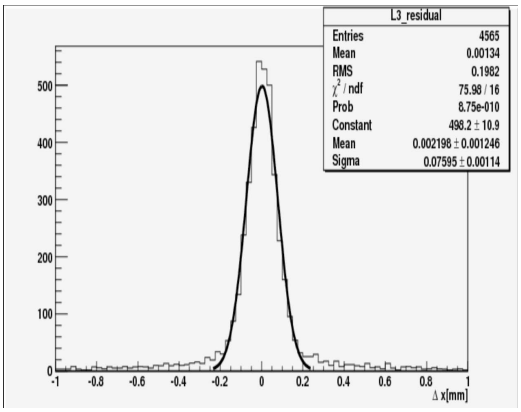

Figure 18: Typical residual for one of the layers with respect to the fitted line.

Finally, by using the Time-over-Threshold method, one can reject single gas-gaps measurements, polluted by a δ-ray, a γ or a neutron-conversion, by demanding less than six strips in a

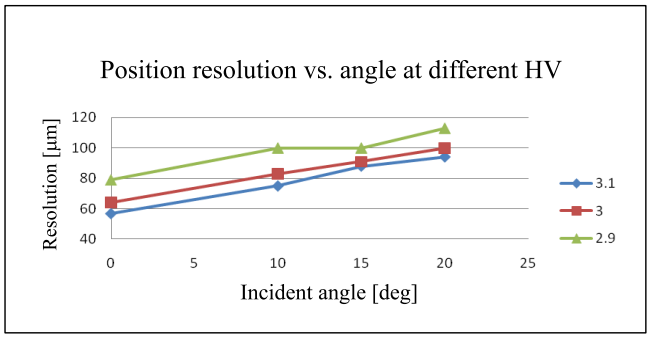

Figure 19: Resolution vs. incident angle as measured with muons in H8.

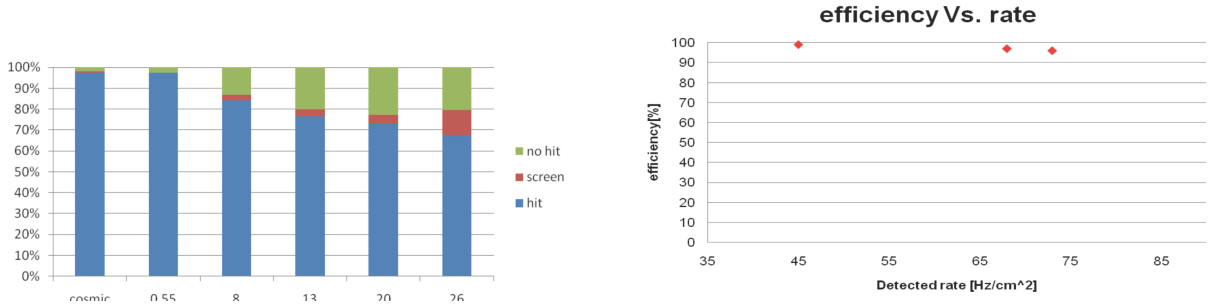

Figure 20: Left: Single layer efficiency in kHz/cm^2 on a large chamber under uniform γ-irradiation (strip length= 1.2 m). Right: Single layer efficiency for MIPs under 5.5 MeV neutron irradiation.

cluster and a cut on the ToT. This is illustrated in Fig. 21, where one can see the passage of a muon through the four gas-gaps, (a) without contamination, (b) with a δ-ray in layer one and (c) with a neutron impinging in layer three.

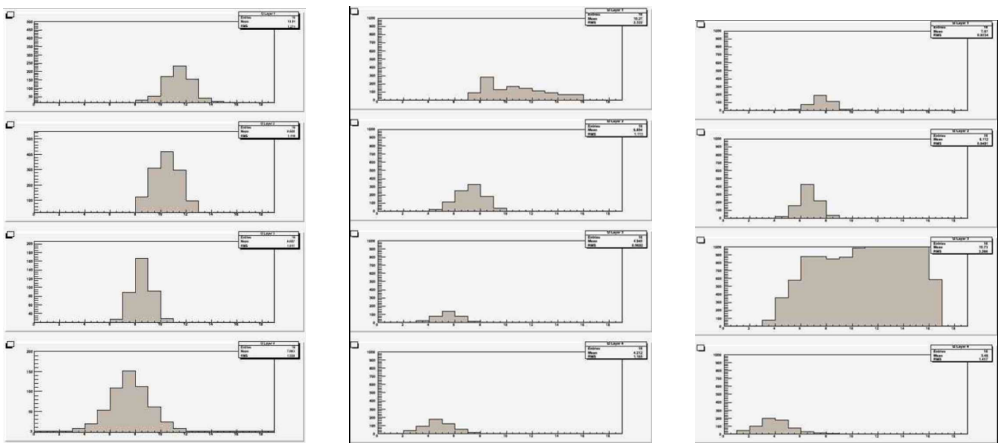

Figure 21: Event display of a) a clean muon track, b) a muon track with a δ-ray in the first gas-gaps and c) a neutron interacting in the third gas gap. The unit of the horizontal axis is 25 ns/division.

5.3.2 Performance of the sMDT tracking chambers

The outer region of the ATLAS detector, where the muon chambers are located, receives high rates of low-energy neutrons, mainly due to shower leakage from calorimeters and shielding structures in the high-η region. At the nominal luminosity, gammas from neutron capture and related conversion electrons are expected to generate hit rates in the range 50–300 kHz in each MDT tube. A conversion electron may create an inefficiency if the signal arrives *before* the muon signal. The muon detection efficiency thus becomes $\exp(-\tau \times f) \approx 1-\tau \times f$, where τ is the average drift time in the MDT tubes and f the hit rate due to gamma conversions.

At high rates of n/γ background, the efficiency may be further reduced by a decrease of the gas amplification due to space charge from slowly drifting positive ions in the tubes, while the *fluctuations* of the space charge tend to degrade the spatial resolution by up to about 20 % at the highest rates.

The effects of gamma conversions in the MDT tubes have been studied in detail using a muon beam in the presence of intense γ-irradiation of up to about 1 kHz/cm^2 500 kHz/tube delivered by the Gamma Irradiation Facility at CERN (GIF) [10]. The results allow to define the baseline of a chamber design with much improved tracking capability: MDT drift tubes with only half the tube diameter offer a reduction of the drift time by a factor 3.5, due to the non-linear relation between track distance from the central wire and drift time (r-t relation) and in addition by a factor 2 from the exposed area, thus yielding a factor 7 in the reduction of the hit rate due to n/γ background. Moreover, up to two times more tube layers can in principle be accommodated in the available space, leading to improved track finding efficiency and position resolution (see Fig. 3).

In order to verify the performance of the 15 mm diameter ("small") drift tube chambers, tests of the full-scale prototype chamber with 2 x 8 layers of 15 mm diameter drift tubes have been performed in the H8 high-energy muon beam in 2010 and 2011 together with integrated TGC chambers (see Fig. 22, left) and, using cosmic ray muon tracks, at the GIF in the presence of adjustable γ background rates of up to 8.5 kHz/cm^2 and 1200 kHz/tube in 1 m long tubes from a 500 GBq ^{1}37Cs source (see Fig. 22, right) [11]. The maximum γ flux corresponds to a background hit rate of 17 kHz/cm^2 in 0.5 m long tubes as they are in the highest background region at the inner radius of the NSWs. The standard ATLAS MDT readout electronics was used with the adjustable deadtime set to the minimum value of 200 ns.

A tube along the track is called "efficient" if the hit is detected inside a 3σ road of the track reconstructed in the other tube layers of the chamber serving as reference. The drift tube resolution is determined by an iterative method described in [21].

Fig. **??** shows the efficiency of small and large tubes vs. hit rate from gamma conversions. As expected, small tubes provide a much better performance at high background rates. The efficiency at rate zero deviates from 100 % due to tracks passing across or close to the tube walls and due to δ-electrons shifting the hit position outside the 3σ acceptance road. The average position resolution in the small tubes was about 120 μm which, due to strong suppression of space charge effects, shows little dependence on the background rate.

As a measure for evaluating the tracking efficiency, we define the "3σ-efficiency" as the

Figure 22: The test setup in the H8 test beam (left) and in the GIF (right).

probability of detecting a tube hit within a distance of 3 times the drift tube resolution σ from the muon track, the muon track being defined by the other tubes on the track, extrapolated to the active volume of the tube. Similarly, the drift tube resolution as a function of the drift radius is determined by an iterative method excluding the evaluated tube from the track reconstruction in the chamber [21].

Figure 23: Efficiency versus background hit rate as measured at the GIF.

Fig. 36 shows the average 3-σ efficiency of 15 mm diameter drift tubes and the track segment reconstruction efficiency of the prototype chamber as a function of the γ background flux in comparison with the results for the 30 mm diameter tubes from previous tests of a BOS MDT chamber in GIF [12], [13]. At low background rate, the 3σ tube efficiencies of 30 and 15 mm diameter tubes are 94 % and 96 %, respectively. The efficiency loss is due to δ-rays created by interaction of the muons with the tube walls which produce hits earlier than the muons. The degradation of the efficiency with increasing rate follows the predicted behaviour. The redundancy of track measurements in the different drift tube layers is sufficient to achieve almost 100 % track segment reconstruction efficiency up to the highest background rates.

Figure 24: Spatial resolution of large and small tubes in the H8 test beam together with simulation results.

In Fig. 37 the spatial resolutions of 15 mm and 30 mm diameter drift tubes measured without background irradiation in the high-energy muon beams H8 and X5, respectively, at CERN as a function of the drift radius r. The latter is determined using an external reference, the other drift tube layers of the prototype chamber in the H8 beam vs. a silicon strip detector beam telescope in the X5 beam. The radial dependence of the 15 mm diamter tube resolution agrees with the 30 mm diameter tube resolution measurement for $r < 7.5$ mm as expected. The average resolutions including time-slewing corrections of 15 and 30 mm diameter tubes at low background rates are 110 ± 10 μm and 80 ± 5 μm, respectively.

5.4 L1 trigger and electronics

The strip signals in the sTGC of the NSW are used to extrapolate tracks to the Big Wheel where the Sector Logic corroborates it with the existing 2-out-of-3 and 3-out-of-4 coincidences in the Big Wheel chambers. The fine granularity of the extrapolation results in high efficiency for trigger rejection. The logic added to accomplish this must not cause the latency to the Sector Logic to exceed 1.05 μs. A detailed breakdown of the sTGC trigger latency is given in the appendix (C.1).

The sub-sector of the extrapolated muon is found as follows: In the two sTGC packages of the NSW, a local trigger is made from two sets of 3-out-of-4 coincidences, corresponding

to a tower of two times 4 pads. Pads in alternating layers are shifted by half a pad in both dimensions to give a 4 times higher granularity of logical towers. The triggering tower selects the strips in its region for transmission to 8 centroid finders, one for each layer. This selection leads to a 20-fold reduction in the number of strips to be processed as well as in the number of centroid finders. The four centroids in each sTGC package are averaged to give two points in 3-D space, defining a vector which points to a sub-sector in η, ϕ of the Big Wheel. The $\tilde{60}$ μm together with their distance of 250 mm provides an angular accuracy of better than 0.3 mrad. A block diagram of the sTGC trigger logic is shown in the appendix (C.1). A demonstrator has been implemented from commercial components to verify the simulated behaviour, in particular the resulting latency of the trigger logic. Each pair of sTGC chamber packages has its dedicated trigger logic. The extrapolation of the track vector to the Big Wheel can be very fast, using a Look-up-Table (LUT).

Some details about the centroid finding strategy:

- The centroid finder currently calculates the centroid from the charge on five strips.
- The charge on each strip is approximated by the Time-over-Threshold (ToT), which is currently measured in steps of 1 nsec and with a 8-bit dynamic range. Optimized parameters will depend on the final ASD characteristics.
- Centroids are included in the average only if the number of strips above threshold is below a certain maximum value in order to exclude δ-rays and conversions (see 21).
- To compensate for time differences in signal routing and particle time-of-flight, strip signals can be delayed in steps of 1 nsec, up to 25 nsec, with groups of 16 strips sharing a delay parameter.

ASD

The baseline is to use BNLś VMM Front End chip, now under development, including both an ASD and readout logic. The planned parameters of this chip (see table) match the needs of the sTGC detectors. The first prototype chips of the Front End will be available at the end of 2011. The sTGC version of this ASD has LVDS outputs suitable for the ToT trigger logic.

Division into On-chamber and Off-chamber Logic

We seek to minimize the amount of on-chamber electronics, because access and power is limited, and on-chamber electronics must be radiation tolerant. Therefore, ASICś in radiation tolerant technology may be preferable over reprogrammable FPGAs.

The row selector, driven by the pad tower coincidence, reduces the number of channels to be read out to the off-chamber electronics by a factor of about 20. This selector and the pad coincidence must clearly be on chamber. The channel delays depend on the channel, so they must be before the selector. If the Time-over-Threshold (ToT) logic is done on-chamber, the bandwidth needed between on and off chamber electronics is much reduced, since 100 bits of

1 ns signal samples are reduced to an 8-bit ToT. To do this reduction, however, the ASICś must be more complex. On the other hand, if placed off-chamber, more bandwidth, meaning more links, fibers and probably more serializer power, is needed, while the radiation tolerant electronics is simpler. The final decision on this optimization will be taken when details of radiation tolerant ASICs and of serializer speeds and power are better known. The centroid finding through calculation of the Big Wheel sub-sector will be done in off-chamber FPGAs.

Latency (calculation, measurement with demonstrator)

A detailed discussion of the latency expected for the sTGC readout is presented in the appendix (C.1).

Compatibility with Phase II upgrade

The pipelines and derandomizers will be designed to handle a 500 kHz Level-1 trigger rate and to accommodate up to 10μs Level-1 latency.

Time schedule for the sTGC electronics development

The schedule for prototyping, development and production of the sTGC trigger electronics is given in the appendix C.2, Table 15.

5.5 Readout Electronics of the MDT and integration in DAQ

The readout of the Small MDT tubes will follow the proven architecture of the present MDT system. A number of additions and modifications, however, will be necessary in order to adapt the rate capability of the readout chain to the requirements of the SLHC. For the mechanical integration of the readout electronics with the Small tube chambers, the layout of the electronics will have to be adapted to the 4 times higher tube density at the ends of the Small tube chambers. Finally, the radiation tolerance of all components will have to comply with the high radiation levels, in particular at the inner border of the Small Wheel.

5.5.1 Architecture of the present MDT readout

In the present readout scheme tube signals are routed via a PCB ("hedgehog card") to a piggy-back card ("mezzanine card"), containing an Amplifier and Shaper, followed by a Discriminator with adjustable threshold, all three functions being integrated in a radiation tolerant ASIC (ASD). The discriminator outputs, in turn, are routed to a TDC, where each leading and trailing edge signal receives a high-precision time stamp, which is retained, together with the corresponding channel number, in a large internal buffer of the TDC ("Level-1 buffer").

When the TDC receives a Level-1 trigger, a subset of the recorded hits, corresponding to a pre-defined time window, are retained for readout and are forwarded to the data concentrator of this chamber, the "Chamber Service Module" (CSM). From there, data are sent to the off-chamber electronics in USA15, the "Readout Driver" (ROD). A CSM can serve up to 18 mezzanine cards. The operation parameters of the analog frontend (ASD) and the TDC are controlled by a JTAG string, which is distributed by the Detector Control System (DCS) to the CSM, which sends it individually to each mezzanine card. Fig. 25 gives the layout of the present system. A detailed presentation of the MDT readout electronics is given in [5]. The ASD and TDC ASICs are described in [7] and [8].

Figure 25: Schematic diagram of the present (left) and of the future MDT readout chain (right). The Chamber Service Module (CSM) collects all data of a given chamber and sends them to the ROD via an optical link. Up to 18 TDCs can be serviced by a CSM. The 40 MHz clock and the Level-1 trigger are broadcast by the TTC system to the TDCs.

5.5.2 Architecture of the readout for MDTs with Small tubes

For the evolution of this architecture into matching the requirements of the Small tube readout, a number of problems limiting the performance of the present scheme has to be overcome. Given the high rate capability of the Small MDT tubes, the bandwidth of the readout system has to be increased. Due to the limitations of the internal buffering scheme and processing speed, the present TDC can only handle average tube rates up to about 300 kHz per tube without losing data, while Small tubes would operate beyond 1 MHz per tube. Therefore, an improved TDC is an essential requirement for a new readout design. Another limitation of the readout bandwidth comes from the optical link, connecting the CSM to the ROD, as the S-link protocol only supports a usable bandwidth of 1,4 Gbit/s. Fig. 26 shows occupancy and efficiency of Large and Small tubes as a function of tube hit rate.

When upgrading the performance of ASICs (ASD, TDC), we have to take into account that their technologies are no longer supported by industry. The following new components had therefore to be introduced into the readout system.

Figure 26: Three performance parameters for the 15 mm MDTs as a function of the tube hit rate. Red curve: efficiency, assuming a dead time of 200 ns (equal to the maximum drift time) after each hit. Blue: Saturation of the data link from TDC to CSM. Purple: Saturation of the link from CSM to ROD. The links have a useful bandwidth of 80 Mbit/s and 1,4 Gbit/s, respectively. Both have a base load of about 15% due to the overhead of the transfer protocol.

(a) The ASD is re-designed in the IBM 130 nm technology. Most analog parameters of the previous design are preserved. A 4-channel prototype, demonstrating the analog parameters, has already been produced and tested and works correctly. The 4-channel version of the complete ASD chip has been delivered in September 2011.

(b) The TDC will be replaced by the HPTDC, designed by the CERN-MIC group ([6]). This 32-channel device has an improved internal buffering scheme as well as higher transfer and processing speeds.

(c) The CSM collects data from a MDT chamber formats the event and sends data, trigger-by-trigger, via an optical link to the ROD in USA15. All logical operations are performed by an FPGA, which will need to be upgraded to higher radiation tolerance. The interface to DCS, needed for controlling electrical and temperature parameters on the chamber will be done via the GBT (see below). The adapter box to the CANbus (ELMB) can therefore be dropped, reducing complexity of cabling.

(d) The link connecting the CSM to the ROD will be replaced by a GigaBit Transmitter link (GBT), developed by CERN. This link provides a 3 times higher transfer rate (Gbit/s), compared to the S-link [9].

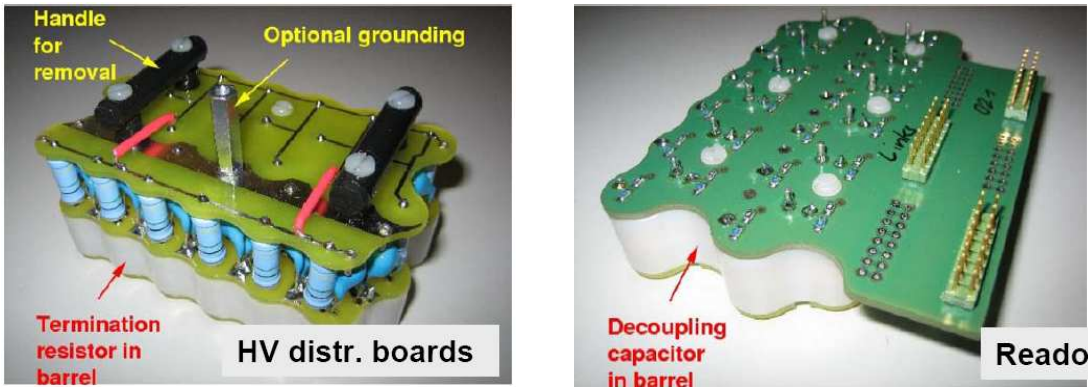

Figure 27: High voltage (left) and signal distribution boards (right), the "hedgehog cards", to be mounted at the two ends of the tubes.

Another stringent requirement for the realization of the new readout scheme is the mechanical integration of the on-chamber readout electronics with the chamber mechanics, as the density of channels at the tube ends is four times higher than in the case of the Large tubes. The following design changes will therefore be implemented.

(a) HV decoupling capacitors are located in 15 mm diameter cylinders at the tube ends, see Fig. 27. The density of signal routing on hedgehog cards is thus no longer limited by HV insulation distances between HV and signal traces on the PCB.

(b) To match the higher tube density, the space on the mezzanine card has to be used more efficiently. For this purpose, the passive protection circuitry of the ASD inputs will be moved to the hedgehog card. In addition, the modularity of the ADSs will be changed from 8 to 16 channels per chip, which goes well with the 32-channel modularity of the HPTDC.

(c) For the interconnection between mezzanine cards and New CSM we foresee to use the same 40-wire cables as was used in the present system. Its moderate diameter and high flexibility may be important for fitting the new MDTs into the limited space in the Small Wheel.

Power consumption of the electronics

While the power consumption of the on-chamber frontend electronics of the present system is about 30–40 W/chamber ([5], table 3), the consumption will now be about 2.5 times as higher due to tube density and increased consumption of TDC, optical link and other component.

A detailed breakdown of the expected power consumption of the MDT chambers in the NSW is presented in Table 7. The total power consumption of 8.8 kW is less than the consumption of the presently installed CSC (11.5 kW, see [2], Table 46). Yet, the removal of the heat may require flushing with dry air, as significant temperature gradients may influence the spatial resolution of the MDT in an uncontrolled way and natural air convection is reduced by the tight space constraints in the high-η region of the Small Wheel.

Chamber type	mezz.s/ chamber	current/ mezzan.	current/ CSM	current/ chamber	power/ chamber at 3.3 V	power/ chamber at 4.5 V
		A	*A*	*A*	*W*	*W*
EIL0	36	18	3	21	69.3	94,5
EIL1	24	12	1.5	14	44.6	60.8
EIL2	32	16	3	19	62.7	85,5
EIS0	40	20	3	23	75.9	103.5
EIS1	28	14	3	17	56.1	76.5
EIS2	24	12	1.5	14	44.6	60.8
Power per Large + Small sector [W]					353	482
Power per side [W]					2825	3852

Table 7: Power requirements for the readout electronics of the NSW. Mezzanine cards and CSMs with 24 channels will be used. Voltage regulators on CSM and mezzanine boards define the nominal 3.3 V from the incoming 4.5 V.

5.6 Services, infrastructure, and DCS

1. *Description of service scheme (including power system, read-out, trigger, alignment), cooling needs and other special requirements*
2. *Table with number of services (number of cables, outer diameter, cross section of leads)*
3. *Table with power consumption (per channel, chamber, total)*
4. *Required rack space*
   (a) *UX15 (include maximum allowed distance to detector if any)*
   (b) *US15 (power system)*
   (c) *USA15 (DAQ)*
5. *Gas system and distribution*
   Details on number of gas manifolds per sector (include drawings) and connections to

chambers (serial, parallel?)). Size of pipes
Required nominal, minimum, and maximum flow
Required precision of gas mixture
Safety measures in case of inflammable gas
Required rack space for gas system in SGX1, USA15, UX15

6. *Integration in DCS system, requirements for DCS !!! Via GBT or ELMB++ ?? !!!*

Gas system and distribution The gas system is a natural extension of the present TGC gas system, which will be extended from the present eight manifolds (four for EIL4 TGCs and four for the SW TGC chambers) to one containing 20 manifolds (four for the EIL4 chambers and 16 for the new Small Wheel chambers (one/layer for the upper and similarly for the lower chambers). This will be less than the normal manifolds in the Big-Wheels and can be easily be added to the present SW racks. The manifolds will be running at a flow rate of 40l/hr of the regular TGC gas mixture, which corresponds to a volume exchange every four hrs. The extra flow corresponds to a 25% increase to the present TGC gas flow, which can be implemented in the present gas system, without any additional modifications, except the extra flowmeters in the present SW racks. The safety system for the new detectors will be the same as for the present one, that were approved by TIS.

Integration in DCS system, requirements for DCS

- Chamber charge monitor
- HV control and monitoring, trip recovery
- LV power control and monitoring
- Temperature monitoring
- Link health statistics
- ASD configuration parameters (threshold, peaking time, etc.)
- Front End trigger and readout configuration parameters (delays, channel masks, pipeline depth, etc.)

6 Expected muon performance with NSW [sv]

Discussion of overall performance. L1 trigger, muon reconstruction, efficiency, fake, sensitivity to a few layout parameters (number of layers, ...),

Cable	Number of cables (granularity)	Outer cable diam. (mm)	Cross section of leads (mm^2))
HV			
LV			
Monitoring and control			
Front-end links			
Calibration			
Alignment			
Miscellaneous			

Table 8: Example table number of services per chamber

Chamber	Number of channels	Power consumption per channel	Total power consumption

Table 9: Example table: Number and types of chambers per sector

7 Integration, assembly and commmissioning [JD]

8 Cost, resources and schedule [LP, TK]

9 Conclusions

Appendices

A Radiation background

Discussion of expected cavern background and its uncertainty based on simulations and measurements with muon detectors, and finally give a reference figures and safety factor.

- *Overview of cavern background. It's nature, origin, shielding strategy*
- *Simulation result. R distribution in the small wheel region. 14 TeV, Al beam pipe, 14 TeV steel beam pipe, 7 TeV steel beam pipe.*
- *Measuremenents with pp collision. MDT, CSC*
- *Summary figure. Reference figures.*

A.1 simulation

B Small-Diameter Muon Drift Tube Detectors

B.1 Tracking in a high–background environment

In order to study the performance of the MDT chambers at high background rates, a full-scale ATLAS BOS chamber has been extensively tested in the CERN Gamma Irradiation Facility (GIF) [12, 13]. The results showed that the drift-tube chambers provide efficient and high-resolution tracking in combination with fast trigger and second-coordinate chambers up to very high occupancies above 20 % [19], which are expected to be reached in the ATLAS endcap muon spectrometer already at twice the LHC design luminosity.

Figure 28: Left: Drift-time spectra of 30 mm and 15 mm diameter drift tubes operated under standard gas and gas gain conditions (see text), normalized to the same area. The measurements with cosmic ray muons for the 15 mm diameter tubes are compared to the Garfield simulation [15]. Right: Space-to-drifttime (r-t) relationship of circular drift tubes operated with Ar:CO_2 (93:7) gas mixture at 3 bar.

Reduction of the outer drift-tube diameter from 30 mm in the present ATLAS Monitored Drift Tube (MDT) chambers to 15 mm while keeping the other parameters, including the gas gain of $2 \cdot 10^4$, the sense wire diameter of 50 μm and the tube wall thickness of 0.4 mm unchanged leads to a significant improvement of the rate capability of the drift-tube chambers which is more than sufficient for their operation in the new Small Wheels up to the highest background rates expected at 5 times the LHC design luminosity. It allows for maintaining the main advantages of the drift tube concept:

(a) High pattern recognition and tracking efficiency up to high backround rates.

(b) High position and angular resolution independent of the angle of incidence onto the chamber plane (in contrast to drift chambers with rectangular drift geometry).

(c) Operational independance of the drift tubes where any malfunction of a tube can only generate a negligible inefficiency.

(d) Modularity and mechanical robustness of chamber construction.

(e) Direct connection of the high intrinsic mechanical precision of the chambers to the global optical alignment system.

(f) Extensive experience in the construction, quality assurance and operation of the MDT chambers in ATLAS; easy integration into the DAQ, trigger and muon reconstruction chains.

The standard MDT operating parameters are kept also for the small-diameter drift tubes (see Table. 10). With the MDT gas mixture of Ar:CO_2 (93:7) at 3 bar absolute pressure, the gas gain of $2 \cdot 10^4$ is achieved at an operating voltage of 2730 V for 15 mm diameter drift tubes.

Parameter	Design value
Tube material	Aluminum
Outer tube diameter	15.000 mm
Tube wall thickness	0.4 mm
Wire material	Gold-plated W/Re (97/3)
Wire diameter	50 μm
Wire tension	300 ± 15 g
Gas mixture	$Ar/CO_2/H_2O$ (93/7/$\leq$ 1000 ppm)
Gas pressure	3 bar (absolute)
Gas gain	2 x 10^4
Wire potential	2730 V
Maximum drift time	$\sim$ 200 ns
Average resolution per tube	$\sim$ 100 μm

Table 10: The operating parameters of small-diameter MDT chambers.

Under these conditions, the maximum drift time is reduced by a factor of 3.5 from about 700 ns to 200 ns by shrinking the tube diameter by a factor of two (see Fig. 28) [14].

In addition, the background flux hitting a tube of given length is reduced by a factor of two. Altogether, the drift-tube occupancy is reduced by a factor of 7. At the maximum background rate of 9 kHz/cm^2 expected at the innermost radius of the Small Wheels at 5 times the LHC design luminosity, the highest occupancy, occuring in the shortest tubes of 0.56 m length at the innermost radius of the Small Wheels, is 15 % corresponding to a counting rate of 750 kHz. 2 x 6 drift-tube layers at radii $R < 2$ m in the Small Wheels and 2 x 4 layers at larger radii provide very robust tracking with track segment reconstruction efficiencies above 99 % at the highest background rates (Fig. 4) [17].

Figure 29: Left: Spatial resolution of 30 mm diameter drift tubes as a function of the drift radius r measured for different background rates at the Gamma Irradiation Facility (GIF) at CERN [13]. Right: Dependence of the average spatial resolution of 30 mm and 15 mm diameter drift tubes on the background hit rate. The results are derived from Fig. 29 by averaging over the tube radius. The gain drop in 15 mm diameter tubes compared to 30 mm diameter tubes is taken into account by multiplying the background rates by the gain reduction factor of 8 (see text).

The space-charge distribution caused by the ion clouds drifting towards the tube wall during a particle crossing modifies the local electric field, influencing both the drift velocity and the gas gain. By lowering the effective potential experienced by the electrons drifting towards the wire, high background flux leads to decreasing gas gain. The resulting signal loss grows with the inner tube radius r_2 proportional to $r_2^3 \cdot \ln(r_2/r_1)$ [16], where $r_1 = 25$ μm is the wire radius, and therefore is about 8 times smaller in 15 mm compared to 30 mm diameter drift tubes. Fluctuations of space charge and electric field lead to variations of the drift velocity causing a deterioration of the spatial resolution in non-linear drift gases like Ar:CO_2 where the drift velocity depends on the electric field. The latter effect increases strongly with drift distance above a value of about 7.5 mm while the gain drop effect on the spatial resolution dominates for distances close to the sense wire (see Fig. 29, left)[18, 12, 13]. For drift radii below 7.5 mm, i.e.

for the 15 mm diameter tubes, the space-to-drift time relationship is more linear leading to a reduced sensitivity to environmental parameters such as gas composition and density, magnetic field and irradiation rate (Fig. 29, right).

Since the spatial resolution of the drift tubes improves with increasing drift radius, the average single-tube resolution, after correction for time slewing effects, is degraded from 80 μm for 30 mm diameter tubes to about 110 μm for 15 mm diameter tubes at low background rates. The average 30 mm diameter tube resolution deteriorates linearly with the counting rate to about 115 μm at 0.5 kHz/cm^2, the maximum background flux expected in the ATLAS MDT chambers at the LHC design luminosity (see Fig. **??**) [13]. Fig. **??** also shows the background rate dependence of the average 15 mm diameter tube resolution as expected from the measured 30 mm diameter tube resolutions given in Fig. 29. The linear deterioration rate of the average 15 mm diameter tube resolution with increasing background flux is about 10 times smaller than for 30 mm diameter tubes resulting in a resolution degradation by only 20 μm at the maximum background rate of 9 kHz/cm^2.

At the highest background rates at 5 times the design luminosity, the point and angular resolutions of the drift tube chambers in the new Small Wheels with 2 x 4 and 2 x 6 tube layers, depending on the radial position, will be uniformly 45 μm and 0.5 mrad, respectively, compared to 40 μm and 0.45 mrad without background irradiation.

B.2 Technical Implementation

B.3 Chamber Assembly

B.3.1 Drift tube production

The drift tubes are fabricated and tested in a climatized clean room of class 10000 using a semi-automated assembly station (Fig. 30). The wires are fed through the tube by air flow without touching them by hand. Wire tensioning and crimping is performed fully automatically. After fabrication, the tubes are immediately tested for wire tension, gas tightness and leakage currents under high voltage (see below).

B.3.2 Chamber assembly

The individual tubes are assembled to chambers using precision jigs on a flat granite table in a climatized clean room as shown in Figs. 31. The jigs are machined with an accuracy of 10 μm. The two multilayers are assembled and glued together within one working day using two identical jigs. The assembly procedure is illustrated in Figs. 32 and B.3.2. The jig elements positioning the endplugs and sense wires of each layer in the transverse plane are stacked layer-by-layer forming a precise two-dimensional grid. Bearings for mounting of the trigger chambers and, for the first multilayer, platforms holding the external alignment sensors are glued to the bottom tube layers positioning them precisely with respect to the assembly jigs and, therefore, to the wires.

Figure 30: The semi-automated drift tube assembly station.

Figure 31: Assembly tooling for the sMDT chambers with precise positioning of the endplugs of the drift tubes holding the sense wires. The jigs are modular and adjustable for the construction of different chamber types. References for the precise mounting of the alignment sensor platforms with respect to the wires are part of the jig design.

On the second day, after letting the glue cure over night, the spacer frame is glued to the top of the first multilayer in its jig and the in-plane alignment system is calibrated. The second multilayer is removed from the jig and glued to the top of the spacer, aligning it precisely with respect to the assembly jig and thus to the first multilayer. Monitoring of the tube and layer positions during chamber construction is not necessary with this assembly scheme.

After the assembly of the drift tubes, the mounting of the gas manifolds and testing for leak tightness requires about one week. Another two weeks are foreseen for mounting of the hedgehog cards, installation of the Faraday cages and cabling of the chamber. Mounting of the trigger chambers on the drift tube chambers and combined test will be performed at CERN.

Figure 32: Assembly procedure of a sMDT chamber. A complete chamber is assembled within two working days.

Figure 33: The sMDT prototype chamber during and after assembly, consisting of two multilayers with 8 tube layers each, 72 tubes per layer and 1152 tubes in total.

B.3.3 Prototype chamber construction

A full-scale prototype of a 15 mm diameter drift tube chamber for the innermost region of the Small Wheels presently covered by CSC chambers has been constructed in 2010 (see Figs. B.3.2 and tested in the CERN Gamma Irradiation Facility GIF as well as in the H8 testbeam in 2010 and 2011. The chamber consists of 2 x 8 layers of drift tubes and is readout with the existing MDT mezzanine cards and Chamber Service Module (CSM). With this prototype chamber all aspects of the chamber design and performance as well as the construction and test procedures have been verified and the required time and manpower for chamber production and test has been evaluated in detail. With the semiautomated drift tube assembly facility, 100 drift tube can be routinely produced per day at each construction site. The tubes assembled every day will be tested for gas tightness and leakage currents under high voltage in automated test stands over night.

The wire positions in the prototype chamber have been measured in the cosmic ray test stand at LMU Munich with an accuracy of few microns. The measured wire grid agrees with the expected grid to better than 20 μm rms (Fig. 34).

Figure 34: The accuracy of wire positioning in the prototype chamber is better than 20 μm rms.

B.3.4 Sharing of work and logistics between production sites

The construction of the 96 drift tube chambers with approximately 70000 drift tubes of lengths between 0.5 m and 2.2 m for the new Small Wheels can be performed at two main construction sites, the MPI Munich and the University of Freiburg, in the years 2013 to 2016. The intergration of the drift tube and trigger chambers at CERN will proceed in parallel.

LMU Munich and the University of Würzburg will contribute to the testing of drift tubes and completed chambers before and after shipment to CERN as well as to chamber integration and commissioning of the Small Wheels at CERN. The relative wire positions of all chambers will be measured with an accuracy of about 10 μm in the cosmic ray test stand at LMU Munich like for the BOS and BOF MDT chambers in ATLAS. With additional institutions joining the project, the chamber construction can proceed faster. 2-3 FTE manpower per construction site are planned for the chamber construction.

The participating institutes have extensive experience with the construction of the ATLAS MDT chambers as well as the associated quality assurance procedures. The required clean rooms and test equipment and the design of tooling for chamber construction and testing already exist. The University of Freiburg and MPI Munich will also be involved in the design, fabrication and measurement of the alignment reference bars for the new Small Wheels in collaboration with Brandeis University.

B.4 Quality Assurance and Commissioning

The quality assurance and commissioning procedures follow closely the specifications for the MDT chamber production for the ATLAS muon spectrometer [20]. Each tubes will be tested for wire tension, gas tightness and leakage currents under high voltage before installation in a chamber. Wire position measurement for individual drift tubes is no more necessary due to the new endplug design (see B.3. Monitoring of the tube positioning in the chamber during assembly has also become unnecessary.

The hedgehog cards and the mezzanine readout boards with the new radiation hard ASD and HPTDC chips as well as the new chamber service modules CSM (see below) will be desiged, produced and tested by MPI Munich. New improved noise filters for the high-voltage supply lines for each chamber layer have been designed and will be produced at MPI Munich.

The completed chambers will be tested for broken wires, gas tightness, leakage currents and noise rate before and after delivery to CERN. In addition, all chambers will be tested in the cosmic ray test stand at LMU Munich and their relative wire positions will be measured with an accuracy of about 10 μm as was done for the BOS and BOF chambers.

After the integration of trigger and drift-tube chambers a measurement of the relative

positions of strips in the trigger chamber with respect to the wires in the drift tube chambers is foreseen. The full quality control procedures have already been developed during the prototype chamber construction.

2-3 FTE manpower at each of the 4 core production sites are planned for chamber testing and commissioning.

B.5 Operation, Maintenance and Safety

Due to their robust design and the high quality assurance standards during construction and commissioning, the ATLAS MDT chambers operate with very high reliability and data taking efficiency. The same design, fabrication and testing procedures will be applied for the small diameter drift tube chambers. Also maintenance and repair procedures will be essentially the same as for the existing MDT chamber system. The foreseen numbers of drift tube layers provide high redundancy. The drift tubes are supplied with separate high-voltage lines layer-by-layer and for each radial segment. If a wire should break, which is a very rare event, only one tube layer has to be disconnected from the high-voltage during short access. During shutdown and and opening of the Small Wheels, the affected tube can be disconnected from the hedgehog cards.

Gas leaks in the installed MDT chambers are due to cracked Noryl® endplugs, damaged gas connections and perforated aluminum tubes. Mechanically, the tubes are protected from the outside by the mounted trigger chambers. To avoid gas leaks due to cracks in endplug insulators and gas connectors thermoplastics with much higher robustness against cracking have been chosen (see B.2, above). In addition, the smaller volume of the 15 mm diameter endplugs are less prone to mechanical stress and cracks introduced by the injection moulding than the 30 mm diameter endplugs.

In the chamber layout and the design of the Small Wheel structure, accessibility of the Faraday cages of the drift tube chambers for exchange of electronics boards or for disconnecting individual drift tubes has been taken into account. The chamber service modules (CSM) of all chambers will be installed in accessible and radiation-safe regions at the outer radius of the Small Wheels.

The existing recirculating gas system with one volume exchange per day can be fully re-used. Each multilayer will be supplied separately with gas using 16 gas lines for each NSW, two for each double-sector of neighbouring small and large chambers. The total gas volume of the sMDT chambers of one NSW is 6750 l, 4000 l less than for the MDT chambers in one present Small Wheel. Each multilayer will be supplied separately with high voltage. 384 HV channels and 96 LV channels (one per chamber) will be needed for the two Small Wheels.

B.6 Performance

In order to verify the performance of the 15 mm diameter ("small") drift tube chambers, extensive tests of the full-scale prototype chamber with 15 mm diameter drift tubes have been

performed in the H8 high-energy muon beam in 2010 and 2011 together with integrated TGC chambers (see Fig. 35, left) and, using cosmic ray muon tracks, in the CERN Gamma Irradiation Facility (GIF) with a 500 GBq $^{1}37$Cs source (Fig. 35, right). The standard ATLAS MDT readout electronics has been used with the adjustable deadtime set to the minimum value corresponding to an overall effective deadtime of 200 ns. The spatial resolution and efficiency of the individual drift tubes and of the whole chamber have been measured for different γ irradiation rates where the individual drift tubes have been illuminated uniformly over the whole length.

Figure 35: The test setup in the H8 test beam (left) and in the GIF (right).

As a measure for evaluating the tracking efficiency, we define the "3σ-efficiency" as the probability of detecting a tube hit within a distance of 3 times the drift tube resolution σ from the muon track, the muon track being defined by the other tubes on the track, extrapolated to the active volume of the tube. Similarly, the drift tube resolution as a function of the drift radius is determined by an iterative method excluding the evaluated tube from the track reconstruction in the chamber [21].

Figure 36: Efficiency versus background hit rate as measured at the GIF.

Fig. 36 shows the average 3-σ efficiency of 15 mm diameter drift tubes and the track segment reconstruction efficiency of the prototype chamber as a function of the γ background flux in comparison with the results for the 30 mm diameter tubes from previous tests of a BOS MDT chamber in GIF [12], [13]. At low background rate, the 3σ tube efficiencies of 30 and 15 mm diameter tubes are 94 % and 96 %, respectively. The efficiency loss is due to δ-rays created by interaction of the muons with the tube walls which produce hits earlier than the muons. The degradation of the efficiency with increasing rate follows the predicted behaviour. The redundancy of track measurements in the different drift tube layers is sufficient to achieve almost 100 % track segment reconstruction efficiency up to the highest background rates.

Figure 37: Spatial resolution of large and small tubes in the H8 test beam together with simulation results.

In Fig. 37 the spatial resolutions of 15 mm and 30 mm diameter drift tubes measured without background irradiation in the high-energy muon beams H8 and X5, respectively, at CERN as a function of the drift radius r. The latter is determined using an external reference, the other drift tube layers of the prototype chamber in the H8 beam vs. a silicon strip detector beam telescope in the X5 beam. The radial dependence of the 15 mm diamter tube resolution agrees with the 30 mm diameter tube resolution measurement for $r < 7.5$ mm as expected. The average resolutions including time-slewing corrections of 15 and 30 mm diameter tubes at low background rates are 110 ± 10 μm and 80 ± 5 μm, respectively.

B.7 Aging Tests

Describe in detail results from aging tests for all components, the detector itself including the on-chamber gas distribution, read-out and/or trigger, alignment, and detector control electronics.

No aging is expected to occur in aluminum drift tubes with clean Ar:CO_2 gas. No aging has been observed in test of the MDT tubes up to a collected charge on the wire of 0.6 C/cm. Endplug and gas system materials with little outgassing which have already been certified for the ATLAS MDT chambers are used and strict cleaning procedures are applied for all components in order to prevent contamination of the drift gas.

Aging tests of the new drift tubes up to 2-3 C/cm collected charge including irradiation of the endplugs are on the way with strong radioactive sources at the accelerator laboratory at LMU Munich.

B.8 Cost, Funding, and Manpower

The costs of chamber mechanical components, on-chamber electronics, power supplies and DAQ system are summarized in Table 11. The cost estimates are based on tenders as well as on the actual cost figures of the ATLAS MDT chamber components.

Manpower cost for chamber assembly and test and for the testing of the electronics boards is not included The manpower allocation foreseen for this work at the participating institutes is shown in Table 12. The infrastructure of climatized clean rooms and the cosmic ray chamber test facility already exist as well es experienced technical personell. The design of the chambers and of the assembly tooling is performed at MPI Munich. The signal and high-voltage distribution (hedgehog) boards, the readout (mezzanine) cards, the amplifier-shaper-discriminator (ASD) chip and the chamber service module (CSM) are already under development at MPI.

A close collaboration exists between the MDT institutes and the TGC as well as the RPC institutes on integrated chamber design and layout and on a common test program at the GIF and the H8 test beam.

It is planned to finance the complete sMDT system from funds by the German funding agency BMBF and by MPI Munich in the period 2012–2016. In addition, NIKHEF has expressed interest to contribute the MRODs. Brandeis University and the University of Freiburg plan to contribute the optical alignment system including the alignment reference bars. The time schedule is shown in Table 13.

References

[1] G. Aad et al. Expected Performance of the ATLAS Experiment - Detector, Trigger and Physics. 2009.

[2] G. Aad et al. The ATLAS Experiment at the CERN Large Hadron Collider. *JINST*, **3** S08003 (2008)

Component	Number units	Cost/unit (CHF)	Total cost (kCHF)
Al tubes	70656	3.6	254
Wire	5.5 km	488/km	3
Endplugs	141312	7.2	1017
Gas connectors/tube	141312	1.8	254
Spacer, supports,	96	1000	96
Gas distribution, valves	2 x 96	300	58
Faraday cages	2 x 98	500	98
Alignment system/chamber	96	600	58
Mechanics			1838
HV&RO hedgehog boards	5888	100	589
Mezzanine cards w. cable	2944	240	706
CSMs (24 ch.)	160	1100	176
DCS modules w. fiber link	160	400	64
On-chamber electronics			1535
LV&HV power supplies w. cables/CSM	160	2000	320
MRODs/CSM	160	1200	192
Services, DAQ			512
Total			3885

Table 11: Cost of the sMDT chambers and DAQ system.

Institute	FTE	Contribution
MPI Munich	5	Mechanics, electronics, L1 trigger design
	7	Chamber construction, test, integration, installation, alignment system, electronics production, HV/LV system
LMU Munich	3-4	Chamber construction, test, integration, installation
Freiburg	5-6	Chamber construction, test, integration, installation, gas system, DCS, alignment system
Würzburg	3	Chamber, electronics test, integration, installation, HV/LV system
NIKHEF		MRODs design, production, test, installation
Brandeis U.		Alignment system

Table 12: Foreseen manpower for sMDT design, production, integration and installation.

[3] M. Bosman et al. Estimation of Radiation Background, Impact on Detectors, Activation and Shielding Optimization in ATLAS, ATLAS Note *ATL-GEN-2005-001* (2005)

[4] P. Barrow, G. Conti, M. Franklin and L. Jeanty, Cavern Background, Muon Upgrade meeting, july, 29th, 2011 *https://indico.cern.ch/congerenceDisplay.py?confId=148910*

[5] M. Deile et al., *Performance of the ATLAS Precision Muon Chambers under LHC Operating Conditions*, Proceedings of the 9^{th} Pisa Meeting on Advanced Detectors, Isola d'Elba, Italy, 25–31 May 2003, Nucl. Instr. and Methods **A518** (2004) 65;
M. Deile et al., *Resolution and Efficiency of the ATLAS Muon Drift-Tube Chambers at High Background Rates*, Proceedings of the 10^{th} Vienna Conference on Instrumentation, Vienna, Austria, 16–21 February 2004, Nucl. Instr. and Methods **A535** (2004) 212;

Time of completion	Task
2010	sMDT Chamber design, prototype construction and test
2011	Integration sMDT amd trigger chambers,
	full ASD FE chip (4 channels)
2012	Construction of sMDT chambers for elevator regions,
	NSW design and chamber layout,
	full 8-channel ASD chip
2014	CSM design incl. MDT based L1 trigger functionality
2013–16	Chamber construction and integration, electronics production
2017–18	Integration and installtion of NSWs at CERN

Table 13: Time schedule for sMDT chamber develoment amd construction.

S. Horvat et al., *Operation of the ATLAS Muon Drift-Tube Chambers at High Background Rates and in Magnetic Fields*, IEEE Transactions on Nuclear Science, Vol. 53, No. 2 (2006) 562.

[6] M. Deile *et al.*, *Performance of the ATLAS Precision Muon Chambers under LHC Operating Conditions*, Nucl. Instr. and Meth. **A 518** (2004) 65; M. Deile *et al.*, *Resolution and Efficiency of the ATLAS Muon Drift-Tube Chambers at High Background Rates*, Nucl. Instr. and Meth. **A535** (2004) 212.

[7] S. Horvat *et al.*, *Operation of the ATLAS Precision Muon Drift-Tube Chambers at High Background Rates and in Magnetic Fields*, IEEE trans. on Nucl. Science Instr. Vol. 53, 2 (2006) 562.

[8] O. Kortner *at al.*, *Alignment of the ATLAS Muon Spectrometer with Tracks and Muon Identification at High Background Rates*, Nucl. Instr. and Meth. **A581** (2007) 545-548.

[9] B. Bittner *et al.*, *Development of Muon Drift-Tube Detectors for High-Luminosity Upgrades of the Large Hadron Collider*, Nucl. Instr. and Meth. **A617** (2010) 169.

[10] R. Veenhof, *GARFIELD: Simulation of Gaseous Detectors, Version 8.01, CERN*, write-up: http://wwwinfo.cern.ch/writeup/garfield.

[11] W. Riegler, *High Accuracy Wire Chambers*, Nucl. Instr. and Meth. **A 494** (2002) 173.

[12] B. Bittner *et al.*, *Development of Fast High-Resolution Muon Drift-Tube Detectors for High Counting Rates*, Nucl. Instr. and Meth. **A 628** (2011) 154.

[13] M. Aleksa *et al.*, *Rate Effects in High-Resolution Drift Chambers*, Nucl. Instr. and Meth. **A 446** (2000) 435.

[14] H. Kroha, *Quality Assurance and Quality Control Reference Document for ATLAS MDT Chamber Construction*, ATLAS Note, ATL-MUON-2000-008, May 1999.

[15] S. Horvat, O. Kortner, H. Kroha, *Determination of the Spatial Drift-Tube Resolution Using Muon Tracks*, ATLAS Note, ATL-MUON-PUB-2006-008, July 2006.

C The TGCs for the New Small Wheel

In this section of the Appendix we present more technical details about the sTGC concept.

C.1 Latency of the sTGC trigger

To be used in phase I of the LHC upgrade, the overall trigger latency must be below a value of 2.55 μs. This means for the sTGC trigger that the signals from the chamber frontend have to arrive at the input of the Sector Logic not later than 1.05 μs after the occurence of the collision at the primary vertex.

The layout of the trigger and readout electronics for the sTGCs is presented in Fig. 38. The delays calculated for each step are listed in Table 14.

A demonstrator for this readout concept has been developed and measurements of the respective latencies will soon be available (39).

Figure 38: Schematic layout of trigger and readout as presently implemented in a demonstrator.

Figure 39: The trigger demonstrator board based on a commercial evaluation board.

	Min (ns)	Max (ns)	notes
TOF from interaction point to SW (10 m)	35	35	
Propagation delay in chamber	25	25	
ASD	10	10	
On chamber cabling (1.5-2.5 m) to selector	8	13	5 ns/m
up- to down-stream package (50 cm)	0	3	
delay for pad trigger and deskew	15	25	
selector	5	10	switch
serializer	5	10	
deserializer	8	16	
Run Length Encoder	16	24	
latency for the last sample of the pulse	64	100	depends on shaping time
find largest signal	7.5	15	
centroid of a layer	13	25	8 layers done in parallel
centroid chooser	5	10	
centroid average	8	15	
tracklet calc (LUT)	8	10	datasheet BRAM access time =2 ns
output serializer	50	75	GBT: 3 clocks
fiber to Sector logic 90 m	495	495	5.5 ns/m
	776	**916**	

Table 14: Latency calculation - The table shows the latency with the insertion of the precision strip trigger logic into the existing path from the Inner Layer coincidence logic to the Sector Logic. We take as a model the Xilinx Virtex6. All numbers are estimates except that for the centroid finder for which a realistic design has been simulated.

C.2 Time schedule for the sTGC project

The schedule for prototyping, development and production of the sTGC trigger electronics is given in Table 15.

Date	Name		
August 2011	Demo-0	Goal	Demonstrate total latency, ASD to Sector Logic input, of pad local trigger, strip selection and sub-sector calculation from centroids in an FPGA.
		Includes	KEK TGC ASDs and Carioca ASDs, 4 layers of 16 strips, 4 layers of 8 or 14 pads, simple non-pipelined readout, based on commercial FPGA eval board
		Excludes	links and fibers, pipelined readout, rad tol technolgy
December 2011	Demo-1	Goal	Add channels to do full 8-layer logic, 64 strips per layer
		Includes	based on purpose built FPGA board
		Excludes	pipelined readout, rad tol technology
February 2012	Demo-1a	Goal	Run with BNL VMM Front End chip (ASD only)
Early 2012			Define on-chamber/off chamber split and choose link hardware. Design on-chamber boards produce rad tol ASICs for on-chamber part 2nd spin of rad tol ASICs design off-chamber boards production of on- and off-chamber boards

Table 15: sTGC trigger development schedule

D RPC

E Micromegas

References

[1] G. Aad et al. Expected Performance of the ATLAS Experiment - Detector, Trigger and Physics. 2009.

[2] G. Aad et al. The ATLAS Experiment at the CERN Large Hadron Collider. *JINST*, **3** S08003 (2008)

[3] M. Bosman et al. Estimation of Radiation Background, Impact on Detectors, Activation and Shielding Optimization in ATLAS, ATLAS Note *ATL-GEN-2005-001* (2005)

[4] P. Barrow, G. Conti, M. Franklin and L. Jeanty, Cavern Background, Muon Upgrade meeting, july, 29th, 2011 *https://indico.cern.ch/congerenceDisplay.py?confId=148910*

[5] Y. Arai et al., ATLAS Muon Drift Tube Electronics, *JINST* **3** P09001 (2008)

[6] J. Christiansen et al., Manual and User Application Notes for the HPTDC, (2004), *http://tdc.web.cern.ch/tdc/hptdc/docs/hptdc_manual_vs2.2.pdf* and *http:/tdc.web.cern.ch/tdc/hptdc/hptdc.htm*

[7] Posch C., Hazen E., Oliver J., MDT-ASD User's Manual, (2007), ATL-MUON-2002-003; *https://edms.cern.ch/document/899037/2/ASD_Manual_vs_2007.pdf*

[8] Y. Arai, AMT-3 User Manual, *https://edms.cern.ch/file/897562/1/AMT3manual_033.pdf, http://atlas.kek.jp/tdc/amt3/AMT3manual_033.pdf*

[9] P. Moreira, find some reference to the GBT!!

[10] M. Deile et al., *Performance of the ATLAS Precision Muon Chambers under LHC Operating Conditions*, Proceedings of the 9^{th} Pisa Meeting on Advanced Detectors, Isola d'Elba, Italy, 25–31 May 2003, Nucl. Instr. and Methods **A518** (2004) 65;
M. Deile et al., *Resolution and Efficiency of the ATLAS Muon Drift-Tube Chambers at High Background Rates*, Proceedings of the 10^{th} Vienna Conference on Instrumentation, Vienna, Austria, 16–21 February 2004, Nucl. Instr. and Methods **A535** (2004) 212;
S. Horvat et al., *Operation of the ATLAS Muon Drift-Tube Chambers at High Background Rates and in Magnetic Fields*, IEEE Transactions on Nuclear Science, Vol. 53, No. 2 (2006) 562.

[11] J. Dubbert et al., *Development of Precision Drift Tube Detectors for the Very High Background Rates at the Super-LHC*, Proceedings of the 2007 IEEE Nuclear Science Symposium, Honolulu, Hawaii, USA, 28 October–2 November 2007; MPI report, MPP-2007-172, November 2007.

[12] M. Deile *et al.*, *Performance of the ATLAS Precision Muon Chambers under LHC Operating Conditions*, Nucl. Instr. and Meth. **A 518** (2004) 65; M. Deile *et al.*, *Resolution and Efficiency of the ATLAS Muon Drift-Tube Chambers at High Background Rates*, Nucl. Instr. and Meth. **A535** (2004) 212.

[13] S. Horvat *et al.*, *Operation of the ATLAS Precision Muon Drift-Tube Chambers at High Background Rates and in Magnetic Fields*, IEEE trans. on Nucl. Science Instr. Vol. 53, 2 (2006) 562.

[14] B. Bittner *et al.*, *Development of Muon Drift-Tube Detectors for High-Luminosity Upgrades of the Large Hadron Collider*, Nucl. Instr. and Meth. **A617** (2010) 169.

[15] R. Veenhof, *GARFIELD: Simulation of Gaseous Detectors, Version 8.01, CERN*, write-up: http://wwwinfo.cern.ch/writeup/garfield.

[16] W. Riegler, *High Accuracy Wire Chambers*, Nucl. Instr. and Meth. **A 494** (2002) 173.

[17] B. Bittner *et al.*, *Development of Fast High-Resolution Muon Drift-Tube Detectors for High Counting Rates*,
Nucl. Instr. and Meth. **A 628** (2011) 154.

[18] M. Aleksa *et al.*, *Rate Effects in High-Resolution Drift Chambers*, Nucl. Instr. and Meth. **A 446** (2000) 435.

[19] O. Kortner *at al.*, *Alignment of the ATLAS Muon Spectrometer with Tracks and Muon Identification at High Background Rates*, Nucl. Instr. and Meth. **A581** (2007) 545-548.

[20] H. Kroha, *Quality Assurance and Quality Control Reference Document for ATLAS MDT Chamber Construction*, ATLAS Note, ATL-MUON-2000-008, May 1999.

[21] S. Horvat, O. Kortner, H. Kroha, *Determination of the Spatial Drift-Tube Resolution Using Muon Tracks*, ATLAS Note, ATL-MUON-PUB-2006-008, July 2006.

[22] G. Conti, P. Barrow, M. Franklin and L. Jeanty, *Cavern Background Studies from MDT*, https://indico.cern.ch/getFile.py/access?contribId=2&resId=0&materialId=slides&confId=151320